

THESIS FOR THE DEGREE OF LICENTIATE OF TECHNOLOGY

Alloy Design for Refractory High Entropy Alloys with Better Balanced
Mechanical Properties at Both Room Temperature and Elevated Temperatures

Xiaolong Li

Department of Industrial and Materials Science

CHALMERS UNIVERSITY OF TECHNOLOGY

Gothenburg, Sweden 2023

Alloy Design for Refractory High Entropy Alloys with Better Balanced Mechanical Properties at Both Room Temperature and Elevated Temperatures

Xiaolong Li

© Xiaolong Li,

ISSN 1652-8891

Technical Report No. IMS-2023

Department of Industrial and Materials Science

CHALMERS UNIVERSITY OF TECHNOLOGY

SE-41296 Gothenburg, Sweden

Tel: +46 765623598

Printed by Chalmers Reproservice

Gothenburg, Sweden 2023

Alloy Design for Refractory High Entropy Alloys with Better Balanced Mechanical Properties at Both Room Temperature and Elevated Temperatures

Xiaolong Li

Department of Industrial and Materials Science

Chalmers University of Technology

Abstract

Motivated by the desire to improve the energy efficiency of gas turbines by operating them at higher temperatures (HT), which will contribute to a more energy efficient and carbonless society, the quest for novel ultrahigh-temperature materials can never be overwhelming. High entropy alloys, the recently emerged multi-component alloys with equiatomic or close-to-equiatomic compositions, are considered highly promising as next-generation ultrahigh-temperature materials. In particular, refractory high entropy alloys (RHEAs), one category of HEAs comprising refractory elements with high melting points, are thought to hold the greatest potential to surpass the current state-of-the-art HT materials, Ni-based superalloys, whose upper bound of service temperature has been limited by the melting point of Ni.

The alloy design of RHEAs for HT applications is highly challenging though. Specifically, how to balance HT strength, room-temperature (RT) ductility and oxidation resistance is a formidable materials challenge. For instance, the solid solution hardening (SSH) strategy has been proved to work nicely to enable excellent HT strength for single-phase bcc structured RHEAs, however, at the cost of losing tensile ductility at RT. Another example is that adding Al, Cr or Si into RHEAs could improve their oxidation resistance, which however harms their RT ductility due to the easy formation of undesirable intermetallics. Innovative strategies to design RHEAs that can meet these demanding materials requirements, i.e., simultaneously possessing excellent HT strength, acceptable RT ductility and excellent oxidation resistance, are desperately in need and constitute the main topic of this licentiate thesis.

Here in this work, the solid solution softening (SSS) strategy was utilized to soften selected RHEAs to achieve RT ductility without compromising HT strength. Minor additions of substitutional transition metals, Mn, Al and Cu, were confirmed to soften a $\text{Hf}_{20}\text{Nb}_{31}\text{Ta}_{31}\text{Ti}_{18}$ RHEA from RT to 1000°C. Further, with the solo Mn additions into a $(\text{HfNbTi})_{85}\text{Mo}_{15}$ RHEA, a concurrent SSS at RT and SSH at intermediate temperatures was achieved, which led to better-balanced mechanical properties at both RT and elevated temperatures. Combining SSS at low temperatures and SSH at intermediate temperatures holds the potential to induce non-zero tensile ductility for those RHEAs with decent HT strength, hence, to deliver desirable mechanical properties required by ultrahigh-temperature materials, and contributes to accelerate the alloy development and engineering applications of RHEAs.

Key words: Refractory high-entropy alloys (RHEAs); high temperature strength; room temperature ductility; temperature dependence of yield stress; solid solution softening and hardening; substitutional solid solutions, oxidation resistance.

Preface

This licentiate thesis is performed at the Department of Industrial and Materials Science at Chalmers University of Technology during the period September 2020-August 2023. This work is funded by Swedish Research Council (grant number 2019-03559) and is carried out under the supervision of Professor Sheng Guo.

List of Appended Papers

Paper I: Xiaolong Li, Jin Lu, Huahai Mao, Hideyuki Murakami, Sheng Guo, Solid solution softening or hardening induced by minor substitutional additions in a $\text{Hf}_{20}\text{Nb}_{31}\text{Ta}_{31}\text{Ti}_{18}$ refractory high entropy alloy. AIP Advanced, accepted.

Paper II: Xiaolong Li, Mao Ding, Qiang Hu, Zhiyuan Liu, Huahai Mao, Sheng Guo, Solid solution softening at room temperature and hardening at elevated temperatures: A case by minor Mn addition in a $(\text{HfNbTi})_{85}\text{Mo}_{15}$ refractory high entropy alloy. Manuscript, submitted.

Contribution to the appended papers

Paper I: The author of this thesis is responsible for the conceptualization, sample preparations and characterization, testing, and data analysis, with the help on high-temperatures hardness investigation from J.Lu and H. Murakami. The work was carried out under the supervision of S. Guo and H.H. Mao. The first draft of the manuscript was written by the author, and the manuscript was revised by all co-authors.

Paper II: The author of this thesis is responsible for the conceptualization, sample preparations and characterization, testing, and data analysis, with the help on room temperatures compression investigation from M. Ding and Z. Y. Liu. The work was carried out under the supervision of S. Guo and H.H. Mao. The first draft of the manuscript was written by the author, and the manuscript was revised by all co-authors.

Table of Contents

1	Introduction	1
2	Definition: from HEAs to RHEAs, a historical perspective	3
2.1	High-entropy alloys (HEAs)	3
2.2	Refractory high-entropy alloys (RHEAs).....	4
3	Roadmap	7
3.1	Strength at high temperatures	7
3.1.1	Solid solution hardening (SSH).....	7
3.1.2	bcc/B2 strengthening.....	12
3.2	Ductility at room temperature.....	18
3.2.1	Valence electron concentration (VEC) engineering.....	19
3.2.2	Transformation induced plasticity (TRIP).....	20
3.2.3	Solid solution softening (SSS).....	21
3.3	Oxidation resistance	27
4	Experimental method	33
4.1	Arc-melting.....	33
4.2	Vickers hardness measurement.....	33
4.3	Oxidation test.....	34
4.4	High temperature hardness test.....	34
4.5	Universal compression test at room temperature	34
4.6	Gleeble compression test at high temperatures	34
4.7	X-ray diffraction	34
4.8	Scanning electron microscopy	35
4.9	Transmission electron microscopy	35
5	Summary of key results.....	37
5.1	Solid solution softening or hardening strategies induced by Minor substitutional addition on soft base refractory alloy --- $\text{Hf}_{20}\text{Nb}_{29.75}\text{Ta}_{29.75}\text{Ti}_{18}\text{-X}_{2.5}$ (X=Mn, Al, Cu, Fe) - (manuscript 1#)	37
5.2	Solid solution softening at room temperature and hardening at elevated temperatures simultaneously induced by minor substitutional alloying: A case by minor Mn addition in a $(\text{TiHfNb})_{85}\text{Mo}_{15}$ refractory high entropy alloy - (manuscript 2#)	39
6	Conclusions and future prospects	43
7	Acknowledgements.....	45
8	References	47

1 Introduction

The quest for new ultrahigh-temperature materials is driven by the need to improve the efficiency of aerospace and power-generation gas turbine engines, by operating at higher temperatures. The hotter the engine, the better[1]! For decades, turbine engines have been heavily relying on the development of state-of-the-art nickel-based superalloys (see Figure 1.1a), which have evolved during a period of 80 years through small incremental changes. Ni-based superalloys have various favorable properties enabling them to operate at high temperatures: high tensile strength and more importantly can retain a high level of strength at high temperatures; sufficiently high ductility to be shaped mechanically; can nicely resist oxidation, creep and fatigue. The materials development for nickel-base superalloys witnesses a steady increase in engine operating temperatures and hence improved performance and efficiency. However, operating temperatures for nickel-base superalloys are now approaching the limit set by their melting temperatures. More specifically, components made by nickel-base superalloys in jet engines can reach temperatures close to 1150°C, just around 200°C below their melting temperatures. Complex cooling systems and protective thermal barrier coatings can enable nickel-base superalloys to exist at higher temperatures, like the gas temperatures within the turbines (close to 1500°C), but this is undesirable at the cost of much reduced efficiency. It is estimated that, if engines can operate without auxiliary cooling at about 1300°C, an almost 50% increase in output power could be resulted [1] (see Figure 1.1b), which greatly motivates the development of new ultrahigh-temperature materials replacing nickel-base superalloys to realize more efficient engines.

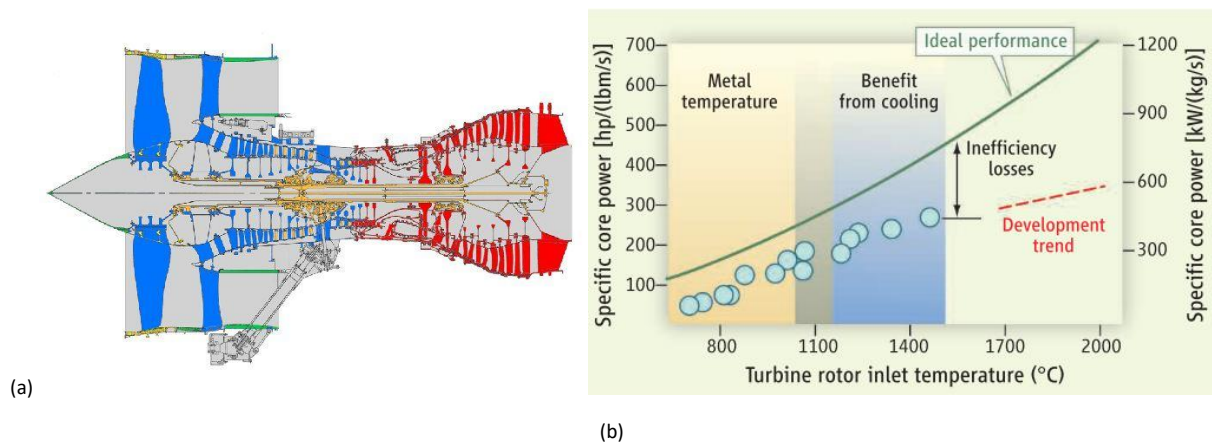


Figure 1.1. (a) Jet engine materials. Components in red are made of nickel-based superalloys where operation temperatures are the highest. (b) Specific core power versus turbine inlet temperature for gas turbine engines. Reproduced from Ref. [1], with the permission of American Association for the Advancement of Science.

Nevertheless, the choices of alternative materials are very limited, due to the numerous demanding performance criteria that need to be met. The foremost criterion is certainly the high melting temperature, which is the preliminary condition for alloys using at high temperatures. Next criterion

is creep property, or the slow deformation under stress, since for example turbine blades are subjected to stress from centrifugal force. Lower creep rate, which is desirable for engine materials, can again be translated into higher maximum operating temperatures. Room temperature ductility enables alloys to be manufactured normally. In addition, the oxidation resistance is another issue considering the working environment of alloys especially when it comes to the high temperatures. Typically, alloys can only obtain one merit at the expenses of the rest two or three, such as the intrinsic ductility-strength trade-off existing in almost all metallic materials. That conflict is exactly behind the rather slow development of high temperature alloys. Currently, there are only a limited number of ceramics, intermetallic compounds and refractory (meaning high melting points) metals/alloys can meet the materials requirements to work at high temperatures. Ceramic and intermetallic compounds have good oxidation resistance and low density, but they tend to suffer from severe embrittlement issues making them unacceptably prone to failure. Refractory metals and alloys, particularly Mo and Nb alloys, are considered as alternative materials which can satisfy many of the requirements for engine applications [2]. Unfortunately, they still suffer from room temperature brittleness and/or insufficient oxidation resistance, with almost no success of achieving ductility after nearly 60 years of intensive research efforts [3]. Thereby, development and exploration of novel ultrahigh-temperature materials which would ideally operate at higher temperatures without the need for auxiliary cooling, will contribute to more efficient turbine engines and less pollution, and to the sustainable energy system worldwide. The ground-breaking concept of refractory high-entropy alloys (RHEAs), which was firstly proposed in 2010 [4], has indeed brought new hopes to push forward this stagnant field, promisingly leading to the development of novel ultrahigh-temperature engine materials.

2 Definition: from HEAs to RHEAs, a historical perspective

2.1 High-entropy alloys (HEAs)

HEAs is a paradigm-shift alloy design concept! Conventional alloys including nickel-base superalloys or steels, are typically based on one principal/major element, like Ni or Fe. The recently emerging new type of advanced metallic alloy, HEAs [5]–[7], however, provides a paradigm-shift in the alloy design strategy that significantly expands the scope for the exploration of new alloy systems and compositions. HEAs typically consist of at least four principal metallic elements in near-equiatomic ratios, and therefore have a higher configuration entropy [8], [9] than that of conventional alloys (This explains why they are termed as HEAs. There are also several different terms used by researchers in the field when addressing HEAs, such as multi-principal-element alloys (MPEAs) and compositionally complex alloys (CCAs) [10], [11]), which can significantly decrease the Gibbs free energy, G , and hence lead to the stabilization of the solid solution phase rather than intermetallic compounds [12], especially at high temperatures, T .

$$G_{mix} = H_{mix} - TS_{mix}$$

Here, G_{mix} , H_{mix} and S_{mix} are the mixing Gibbs free energy, mixing enthalpy and total mixing entropy (S_{mix}), respectively. In the literature, HEAs are claimed to differ from conventional alloys by exhibiting the following four distinct characteristics [13], which are however not all supported by experimental evidence:

1) High-entropy effect:

Compared with traditional alloys with one major element such as Fe, HEAs comprise of at least four major elements with equi- or near equi-atomic ratio, therefore they have high configurational entropy helping to stabilize the solid solution phase. In many cases, a single solid solution phase is formed in HEAs, which is against what the traditional Gibbs phase rule dictates. Most frequently, there are three types of solid solutions that are formed in HEAs, differing by their crystal structures: ① Face-centered-cubic (fcc) solid solution, made from 3d transition metals, such as the Cantor alloy CoCrFeMnNi [14]; ② Body-centered-cubic (bcc) solid solution, made from refractory metals, such as Senkov alloys VNbMoTaW [15] and TaNbHfZrTi [16]; ③ Hexagonal close-packed (hcp) [17] solid solution, mainly made from rare-earth elements.

2) Severe lattice distortion

In HEAs, the concepts of solutes and solvents do not apply anymore. Atomic sizes of constituent elements are different, which makes the lattice position drifting within a certain range thus causes the severe lattice distortion alloys. It was claimed that HEAs will be easily solid solution strengthened (SSS).

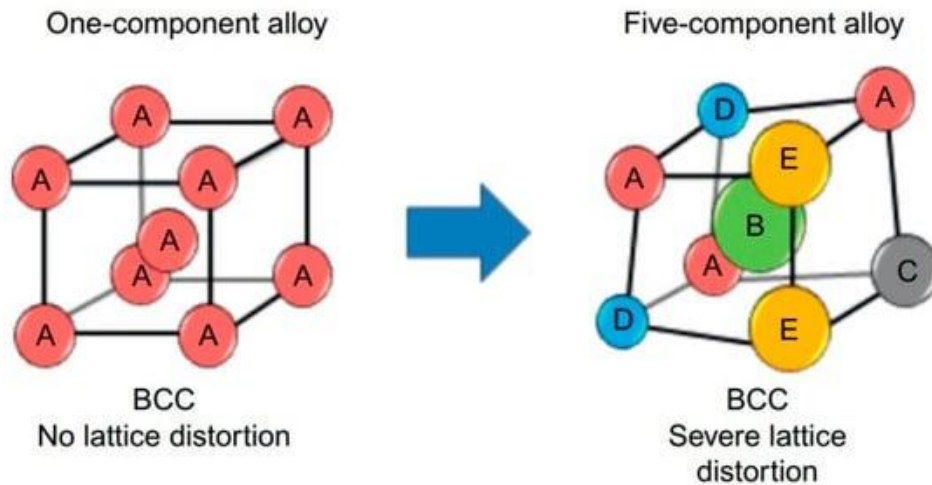


Figure 2.1. Schematic illustration of lattice distortion in BCC-solid solution forming HEAs.

3) Sluggish diffusion

As the lattice is severely distorted, any dimensional defects such as vacancies, dislocations and interfaces, must experience this rough landscape with lattice friction when they want to move, resulting a decrease of diffusional coefficient of elements thus hindering most solid-state phase transformations. This claim is however the most controversial one among the four core effects for HEAs [18].

4) Cocktail effect

Besides all the contributions from individual elements, HEAs might create a complex outcome, even more significant than that of just the simple sum of all constituents.

Due to their unique features notably including high strength, high softening resistance at elevated temperatures and the slow diffusion kinetics, HEAs naturally possess the advantages to be considered as new types of high-temperature materials. If these unique advantages can be further combined with the high melting temperatures from refractory metals, the idea of refractory HEAs would be a highly interesting alloying concept within the context of high-temperature applications.

2.2 Refractory high-entropy alloys (RHEAs)

RHEAs, naturally, are HEAs made from refractory metals (see Figure 2.2 below).

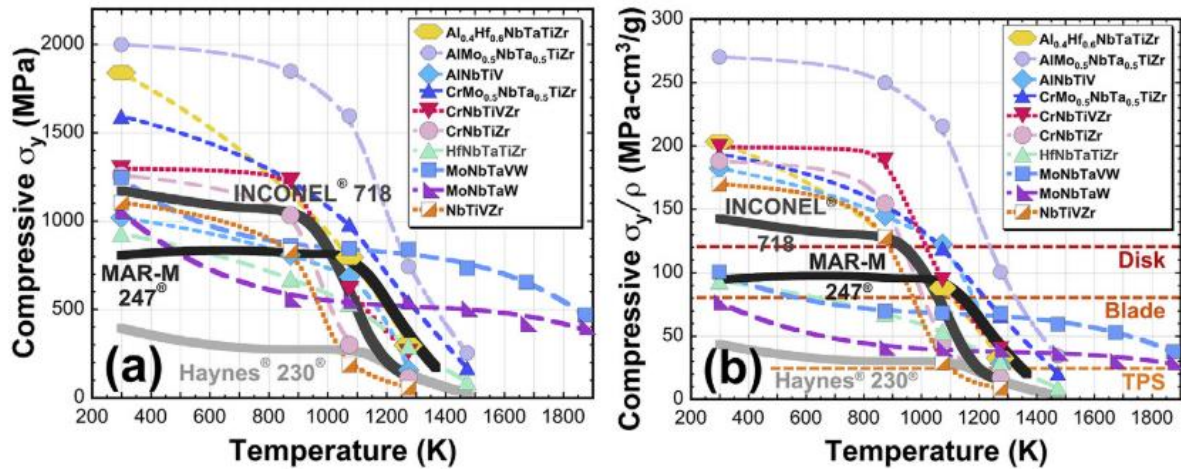
Sc	Ti	V	Cr	Mn	Fe	Co	Ni	Cu	Zn
Y	Zr	Nb	Mo	Tc	Ru	Rh	Pd	Ag	Cd
*	Hf	Ta	W	Re	Os	Ir	Pt	Au	Hg
**	Rf	Db	Sg	Bh	Hs	Mt	Ds	Rg	Cn

Refractory metals

Wider definition of refractory metals

Figure 2.2. Regular definition of refractory metals.

a) The positive side: RHEAs have been paid substantial attention since their first report [15]. Indeed, the firstly developed two RHEAs in 2010, Nb₂₅Mo₂₅Ta₂₅W₂₅ and V₂₀Nb₂₀Mo₂₀Ta₂₀W₂₀ already significantly impressed the materials community in that their yield strength at temperatures above 800°C are much higher than that of some nickel-base commercial superalloys, Inconel 718 and Haynes 230. Today, research activities on RHEAs are among the most pursued ones in the HEAs community. Figure 2.3 ~~错误!未定义书签。~~ summarizes the recent advances in the development of RHEAs, and it can be seen clearly that the compressive yield strength of most RHEAs exceed that of Haynes 230 and some even show potential to extend the use temperature of turbine blades and disks beyond current



superalloys.

Figure 2.3. Temperature dependence of (a) compressive yield strength, σ_y and (b) σ_y normalized by alloy density, ρ , of some representative RHEAs. Tensile σ_y for commercial superalloys (Haynes 230, Inconel 718 and MAR-M 247) are shown for reference. Typical σ_y/ρ requirements for thermal protection sheet (TPS), turbine blades and disks are shown in (b). Reproduced from Ref. [20], with the permission of Elsevier.

It has been experimentally proved that a high yield strength of RHEAs at high temperatures over 1000°C is not hard to get [21]–[24]; and due to the sluggish diffusion resulting from the severe lattice distortion, the diffusion related processes such as creep are expected to be slowed down in RHEAs

which is also quite advantageous for the alloys aiming for use at elevated temperatures. Finally, RHEAs are comprised of metals with metallic bonding, and supposedly they possess some degree of ductility at different temperatures. Not surprisingly, since their discovery RHEAs are believed to hold a great potential to be the next-generation ultrahigh-temperature material.

b) The negative side: Initially, RHEAs suffer from issues like high density, brittleness, and oxidation. Density is not a big issue now, and brittleness is also solvable, but a combination of room temperature (RT) ductility, oxidation resistance and high temperature (HT) strength is quite challenging and has not been achieved yet. Even a combination of two from abovementioned three aspects has been proved extremely difficult. Previous efforts to address the brittleness (via VEC engineering [23], [26] and TRIP [27], [28]) and insufficient oxidation resistance (by alloying and surface treatment [29]–[31]), individually, are briefly summarized in following sections. For structural engineering materials used in the HT environment, they need to achieve a good balance of applicable density, RT ductility, HT strength and acceptable oxidation resistance. Unfortunately, for RHEAs, materials requirements for these various merits are often contradictory, similar to the scenario that is facing conventional refractory alloys [32]–[34]. Notably, one of the bottlenecks for utilizing RHEAs as structural materials has been their RT brittleness. As a matter of fact, the conflict between high strength and high ductility at RT is a general problem for all metallic materials, not only for RHEAs. Basically, single-phase fcc structured HEAs are ductile but not strong enough; single-phased bcc structured HEAs, on the other hand, can be easily very strong but lack of the ductility, particularly under tension, as exactly is the case for bcc structured RHEAs. How to solve the seemingly intrinsic conflict between strength and ductility for compositionally complex RHEAs therefore constitutes a great scientific challenge. Another challenge, and indeed a tougher challenge remains in that the oxidation resistance is required for RHEAs, while keeping the balanced strength and ductility at the same time. In addition, how to efficiently design novel RHEAs with desirable properties is also quite a challenge. Trials and errors are certainly not efficient, if possible, considering the vast compositional space that is opened by the RHEA concept. Combinations with high throughput computational materials design can accelerate the discovery, exploration and development of RHEAs, based on thermodynamics calculations. The great challenges also mean great opportunities, considering the new advances that have been brought by RHEAs in recent years, and the compositional flexibility that is enabled by the RHEA alloy design strategy.

3 Roadmap

There is already a great body of literature reviews summarizing the alloy development and properties of RHEAs. As stated previously, three aspects are most desired for RHEAs, i.e., high strength at HT, tensile ductility at RT, and acceptable oxidation resistance at HT. Ideally, RHEAs shall possess a combination of these three merits, which is however not achieved yet. Therefore, the progresses made on these three aspects regarding RHEAs are summarized separately.

3.1 Strength at high temperatures

3.1.1 Solid solution hardening (SSH)

Solid solution hardening (SSH) caused by alloying, from both interstitial and substitutional additions, is accompanied with the development of HEAs and has been extensively employed for single-phase bcc-structured RHEAs. As shown in Figure 3.1 below, hard but brittle MoNbTaW, MoNbTaVW and ductile HfNbTaTiZr are the most studied RHEA compositions, which all obtain a single-phase bcc structure, and Mo, Nb, Ti, Zr are the most frequently used elements in RHEAs. Given the fact that all refractory metals almost possess the bcc structure or the bcc structure at high temperatures, all RHEAs have the bcc or ordered B2 structure as the matrix, with in some cases several secondary phases such as Laves phase or B2, as shown in Figure 3.2 below.

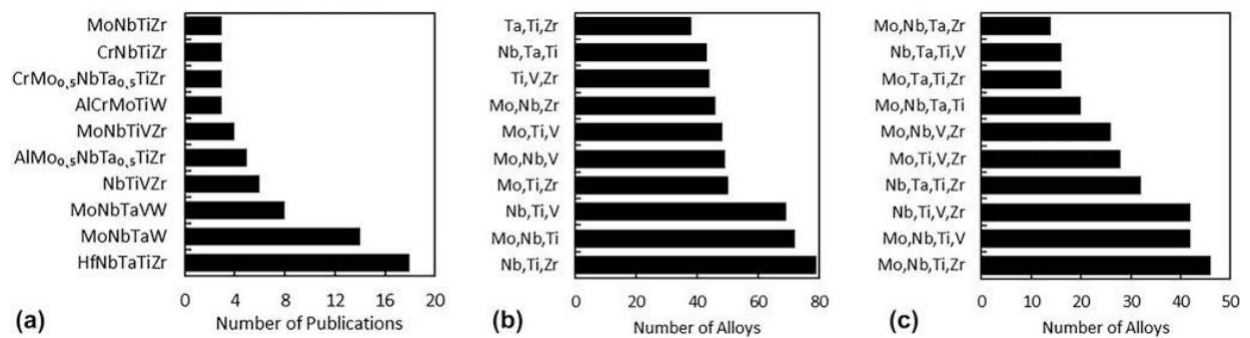


Figure 3.1. (a) Compositions of most frequently studied RHEAs and the number of publications where these compositions were studied. (b and c) Most frequent combinations of (b) three elements and (c) four elements in reported RHEAs. Reproduced from Ref. [35], with the permission of Springer.

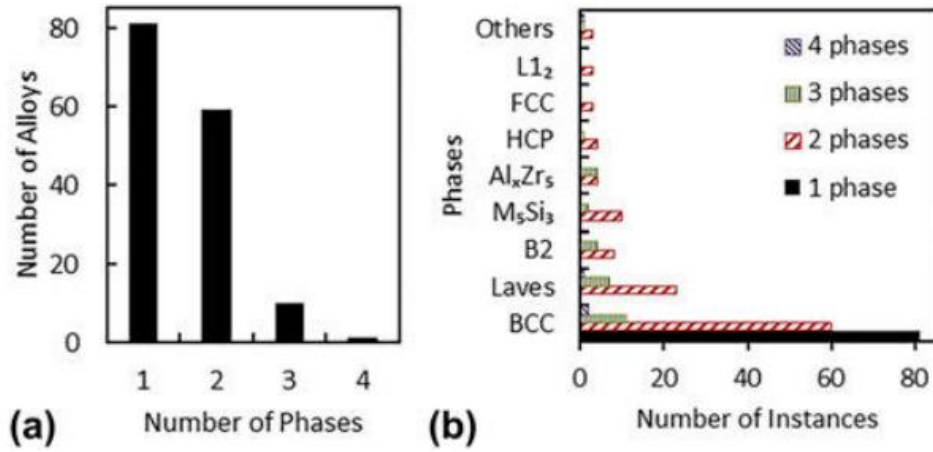


Figure 3.2. (a) Distribution of reported RHEAs by the number of phases. (b) Number of occurrences of different phases in 1-, 2-, 3-, and 4-phase RHEAs. Reproduced from Ref. [35], with the permission of Springer.

The yield strength at RT for some RHEAs is summarized in Figure 3.3, and it can be seen that single-phase RHEAs commonly have an atomic radius misfit parameter $\delta_r < 7.5\%$, and there is no direct correlation between $\sigma_{0.2}^{250^\circ\text{C}}$ and δ_r for these alloys. For most cases at RT, the yield strength from multi-phase alloys is higher than that from single-phase ones, which totally makes sense due to the secondary phase strengthening effect.

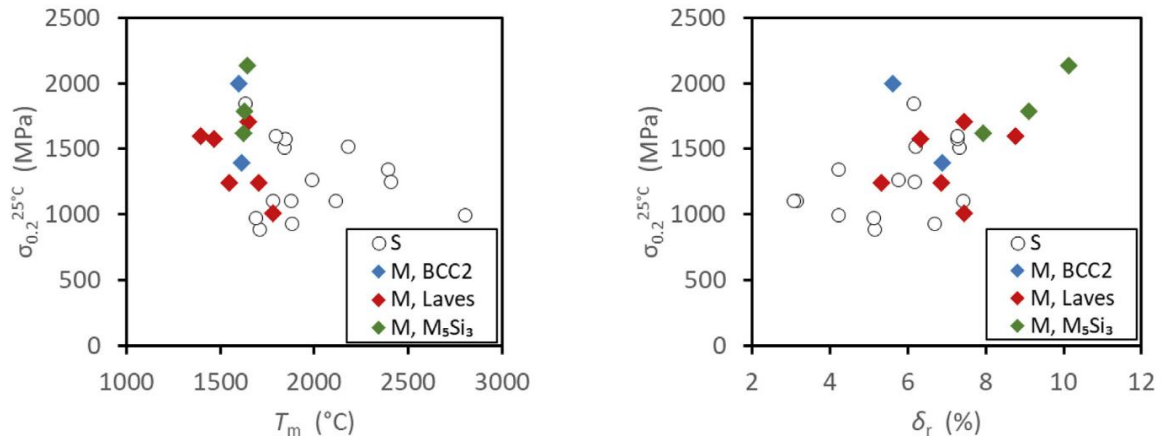


Figure 3.3. Room temperature yield strength ($\sigma_{0.2}^{250^\circ\text{C}}$) of single-phase (S) and multi-phase (M) RHEAs as a function of (a) the alloy melting temperature T_m , (b) atomic radius misfit parameter δ_r . Reproduced from Ref. [36], with the permission of Elsevier.

Regarding the yield strength of RHEAs at HT, as shown in Figure 3.4, there is a clear trend observed in that the single-phase alloys with a higher melting point have a higher yield strength at 1000°C . Furthermore, $\sigma_{0.2}^{1000^\circ\text{C}} / \sigma_{0.2}^{250^\circ\text{C}}$ is proportional to the melting points of these single-phase bcc structured alloys that are listed here. As for the alloys with multi-phases, their HT strengths are randomly distributed and are easy to decline over 1000°C possibly due to the dissolving of other phases at HT [36].

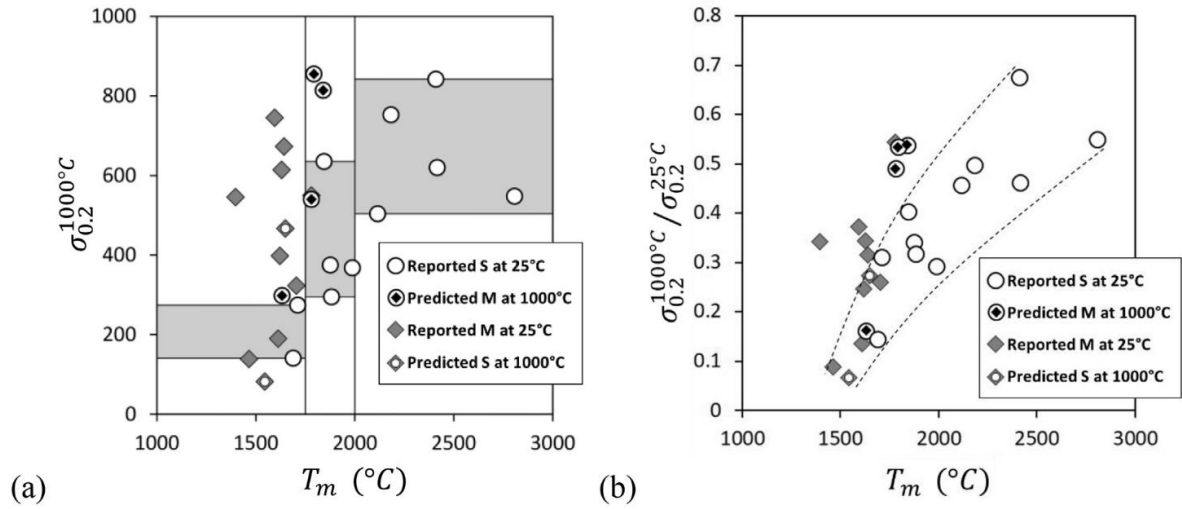


Figure 3.4. (a) Yield strength at 1000°C ($\sigma_{0.2}^{1000^\circ\text{C}}$) and (b) yield strength ratio ($\sigma_{0.2}^{1000^\circ\text{C}} / \sigma_{0.2}^{25^\circ\text{C}}$) of single-phase (S) and multi-phase (M) RHEAs as a function of the melting temperature T_m . Reproduced from Ref. [36], with the permission of Elsevier.

In light of the reviewed literature, as high yield strength at HT is desired, single-phase RHEAs are preferable choices over alloys with multi-phases. As for the solid solution strengthening in bcc-structured metallic materials, it is widely accepted that plasticity is mainly controlled by the motions of screw dislocations [37], [38]. Recently, however, several findings discovered that at intermediate or higher temperatures the movement of edge dislocations plays a non-negligible role [39], [40]. Conventionally, the deformation behavior of bcc material is far more complex than that of fcc materials. The flow stress, which is temperature and strain rate dependent, can simply be divided into three stages as a function of temperature: at the low temperature range (< 0.25 homologous temperature), the flow stress is strongly temperature and strain rate dependent. The motion of the non-planar core of $1/2\langle 111 \rangle$ screw dislocation is thermally activated by double-kink nucleation and can then propagate laterally along the long screw dislocation line when an external shear stress is applied [41]; at the intermediate temperature range (≤ 0.5 homologous temperature), the flow stress is insensitive to the temperature or strain rate. Plasticity is mediated by either the motion of screw, edge dislocations or mixed dislocations passing by the rough landscape resulted from the lattice friction; at the high temperature range (> 0.6 homologous temperature), the flow stress drops quickly due to the increasing impact of thermally activated diffusional processes and is mainly controlled by dislocations climbing. However, in case of concentrated solid solutions, some additional effects have to be taken into consideration, like the pinning mechanism due to fluctuations of local chemical environment, or the formation of super-jogs, as well as the transition from screw to edge dislocation dominated yielding [41]–[44].

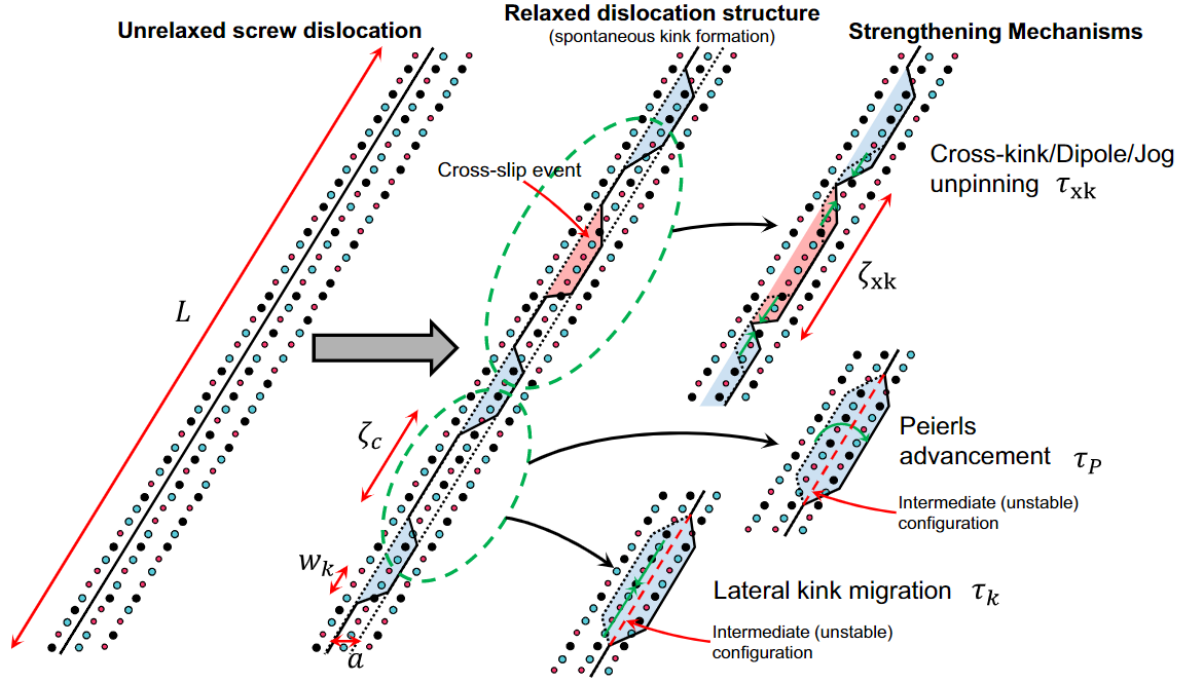


Figure 3.5. Structure and motion of a screw dislocation in a random solute environment. A long straight screw dislocation of length L in a random solute environment assumes a low-energy configuration in which kinks of small width w_k and height a are formed spontaneously and are spaced by a characteristic length ζ_c . The screw dislocation has a symmetric, compact core and thus can kink on any of the three different $\{110\}$ planes containing its line direction. We show two such cases, by coloring regions in blue when the dislocation kinks on one plane (taken here, arbitrarily, as a reference) and in red when the dislocation kinks on a different plane (here called “cross-slip” event). Thus, cross-slip events are merely due to the symmetry of the compact dislocation core. Under an applied stress, lateral kink glide can induce cross-kink (dipole or jog) formation, which causes cross-kink pinning. For segments between two kinks lying on the same slip plane, the segment can advance either by the Peierls mechanism or by lateral kink glide and annihilation. Segment advancement occurs over a characteristic glide length $2a$, going through an unstable, high-energy intermediate configuration. Reproduced from Ref. [37], with the permission of Elsevier.

The solid solution strengthening results from the interaction of elastic stress field between the dislocations and solute atoms [45], [46]. The interaction force, F , increases with both the atomic size misfit parameter, $\delta_a = (1/a) da/dc$, and the modulus misfit parameter, $\delta_\mu = (1/\mu) d\mu/dc$, of the solute and solvent elements [35]:

$$F = \mu b^2 \delta = \mu b^2 (\delta_\mu + \beta \delta_a)$$

Here μ is the shear modulus of the alloy, b is the magnitude of the Burgers vector, a is the lattice parameter, c is the solute atom fraction, and β is a constant, which is in the range from 2 to 4 for screw dislocations and ≥ 16 for edge dislocations [45]. For a concentration solid solution, the solute-induced stress increase $\Delta\sigma$ can be expressed as [45], [47]:

$$\Delta\sigma = A\mu\delta^{4/3}c^{2/3}$$

Here A is a dimensionless constant which is of order of 0.1. This equation was initially developed by Labusch [47] for binary solid solutions in which the concentration of the solvent exceeds 60–70% and modified by Senkov et al. [48] later to apply as the first solid solution strengthening model for RHEAs and tried on the HfNbTaTiZr alloy. The misfit parameters δ_a and δ_u were calculated by averaging nearest-neighbor atom interactions under the assumptions that local concentrations are equal to the average concentration of the alloy. Then, the modified parameters of δ_{ai} and δ_{ui} in the vicinity of an element i can be calculated as [48]:

$$\delta_{ai} = \frac{9}{8} \sum_j c_j \delta_{aij}$$

$$\delta_{ui} = \frac{9}{8} \sum_j c_j \delta_{uij}$$

Here c_j is the atomic fraction of an element j in the alloy, 9 is the number of atoms in the i -centered polyhedron in the bcc lattice, 8 is the number of atoms neighboring with the center atom i , $\delta_{aij} = 2(r_i - r_j)/(r_i + r_j)$, and $\delta_{uij} = 2(u_i - u_j)/(u_i + u_j)$ [35].

Then based on the equations listed above, a direct correlation between the yield stress increase and atomic size with modulus misfit parameters can be established, but still, it falls into the single-phase bcc structure alloys category. One potential issue with solid solution strengthening is this large misfit between either atomic or modulus will increase the risk of decomposition of phase and lower the thermal stability of the alloy in particular at HT. An example of superior high strength of RHEAs at 1000°C designed using this strategy to maximize the misfit parameters is given in Figure 3.6. It was noted that a higher yield strength from the same CrMoNbV alloy could be achieved, when being prepared by powder metallurgy, over the traditional cast counterpart. Therefore, different material fabrication methods are worthwhile to explore, like additively manufacturing for instance. Despite a high yield stress is always a priority, a good balance of ductility at RT and yield stress at HT is the ultimate goal.

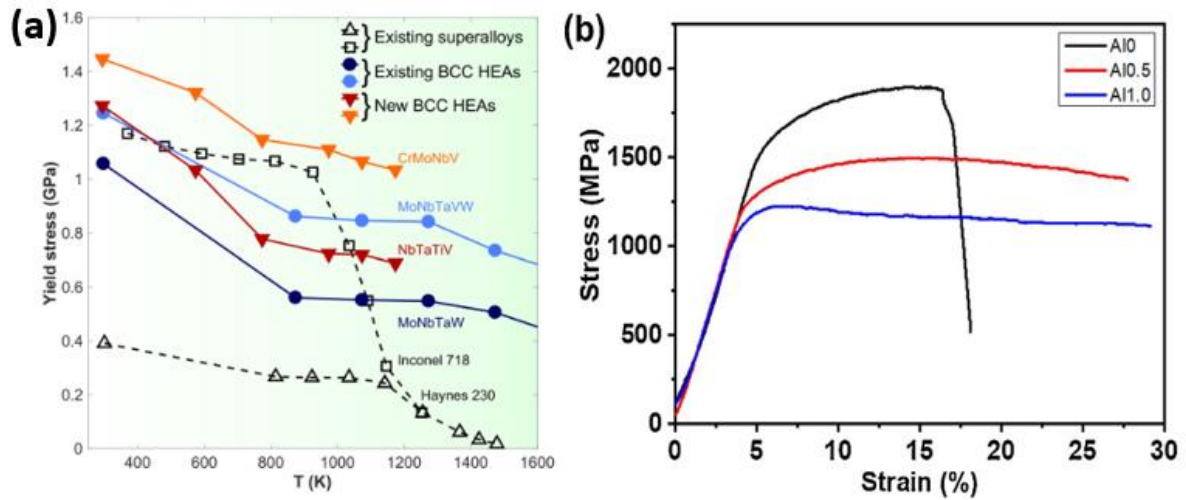


Figure 3.6. (a) The compressive yield stress vs temperature of several high-strength RHEAs, especially CrMoNbV. Reproduced from Ref. [39], Open Access (Nature Communications); (b) compressive engineering stress and strain curves of $\text{Al}_x\text{CrNbVMo}$ alloys fabricated by the powder metallurgy route. Reproduced from Ref. [24], with the permission of Elsevier Science & Technology Journals.

Another aspect in terms of strengthening is about the short-range-ordering (SRO), on atomic pairs mainly associated with the large negative enthalpies, such as Ti group metals associated with interstitial elements like oxygen [49]–[51]. SRO, which is system-dependent, can make a difference not only on the strength but also the deformation behaviors. Therefore, it can be an effective way to overcome the commonly seen tradeoff between strength and ductility. How to engineer an SRO configuration with various degree is challenging. Nevertheless, the concept of HEAs significantly expands the alloy compositions and naturally HEAs become a hotbed for nurturing SROs. These atomic pairings can act as pinning points to affect the dislocation behaviors [52], [53] and alter stacking fault energy [54], therefor can eventually result in different material performance.

3.1.2 bcc/B2 strengthening

From previous reports on multi-phases RHEAs with different secondary phases such as B2, Laves phase and silicides [55]–[57], one combination simulating the typical γ/γ' microstructure in Ni-based superalloys, i.e., the bcc/B2 structural configuration with coherent precipitates sticks out and is showing some promise [58]–[62]. From the very beginning [63], Al was introduced to lower the density, increase HT strength and specific strength, and improve oxidation resistance simultaneously. Another purpose is to see if the Al addition can stimulate or suppress the formation of intermetallic phases in the Ti-Zr-V-Nb-Ta-Mo system. Three compositions, $\text{AlMo}_{0.5}\text{NbTa}_{0.5}\text{TiZr}$, $\text{Al}_{0.3}\text{NbTaTi}_{1.4}\text{Zr}_{1.3}$ and $\text{Al}_{0.5}\text{NbTa}_{0.8}\text{Ti}_{1.5}\text{V}_{0.2}\text{Zr}$ with low density all showed basket-weave, coherent nanolamellar structures inside of the grains of two-phases. bcc structure and also ordered B2 were detected by TEM (Figure

3.7 b). The first composition, $\text{AlMo}_{0.5}\text{NbTa}_{0.5}\text{TiZr}$, had the highest yield strength of 745 MPa at 1000°C over the rest alloys, making it very competitive and got substantial attention since its discovery.

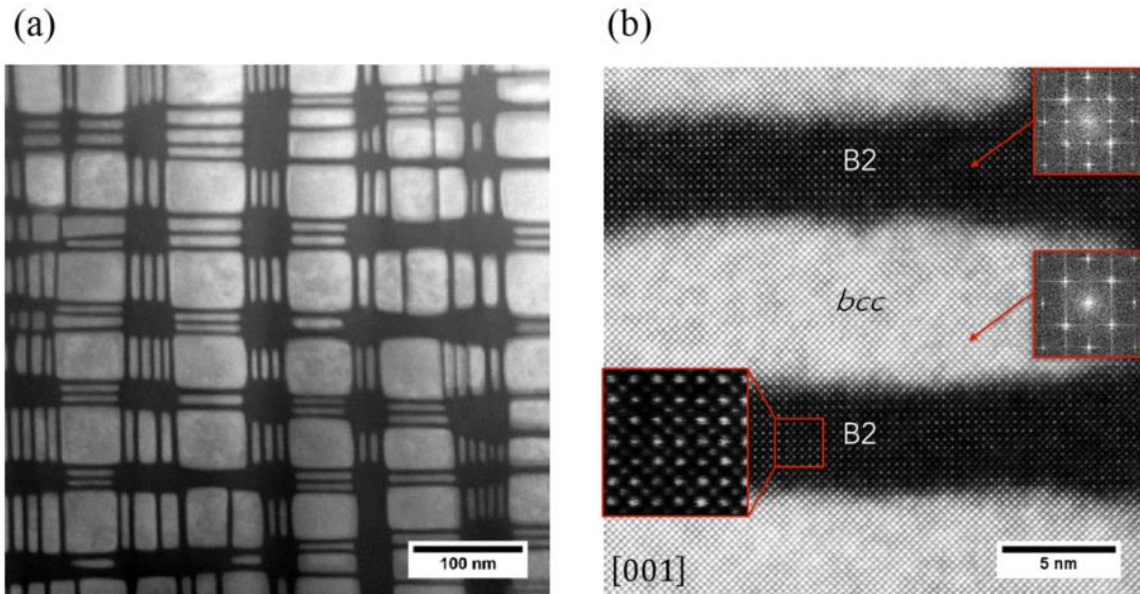


Figure 3.7. STEM-HAADF images of nanostructure present inside the grains of $\text{AlMo}_{0.5}\text{NbTa}_{0.5}\text{TiZr}$. (a) Cuboidal precipitate of disordered bcc phase and continuous ordered B2 phase. (b) Fast Fourier transforms reveal an ordered B2 and disordered bcc phase. Reproduced from Ref. [58], with the permission of Springer.

Afterwards, tremendous efforts have been put into this line of research, hoping that this is maybe a potential way to solve the brittleness issue extensively existing in the single-phase bcc structured RHEAs at RT and to retain their high strength at HT at the same time [61]. Again, the popular composition $\text{AlMo}_{0.5}\text{NbTa}_{0.5}\text{TiZr}$ was systematically characterized [59]. The phases were found to exhibit a continuous channeled B2 phase enriched with Al and Zr with a coherent precipitates of discontinuous bcc phase enriched mainly with Nb, Ta (Figure 8) and an orientation relationship was given by $\langle 100 \rangle_{\text{bcc}} // \langle 100 \rangle_{\text{B2}}$, $\{001\}_{\text{bcc}} // \{001\}_{\text{B2}}$.

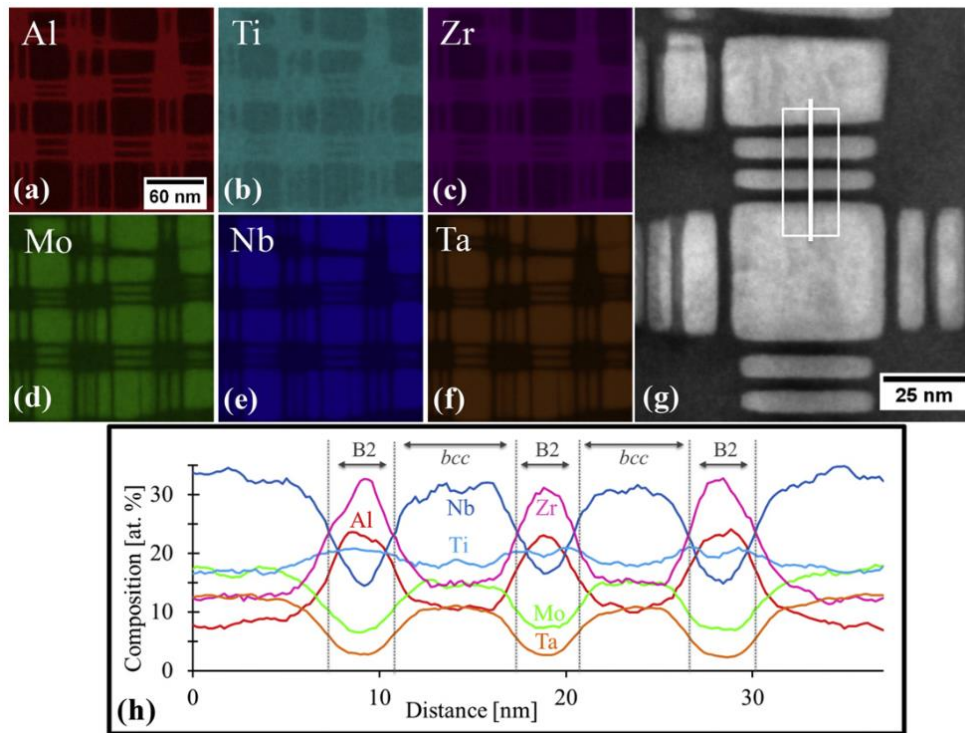


Figure 3.8. (a-f) XEDS elements maps of the $\text{AlMo}_{0.5}\text{NbTa}_{0.5}\text{TiZr}$ alloy. (g) A STEM-HAADF image with a white line identifying the location of the quantified XEDS line-scan shown in (h). Reproduced from Ref. [59], with the permission of Elsevier Science & Technology Journals.

Although the microstructure is analogous to Ni-based γ/γ' superalloys and the specific strength is exceptionally high in the whole temperature range, the alloy is still quite brittle especially at RT. It is noted here that the matrix is the brittle B2 channel and the ductile bcc phase acts as precipitates, which is exactly the opposite component configuration of traditional Ni-based superalloys with a ductile fcc matrix and L_{12} Ni_3Al as the precipitate. Thus, efforts were made on microstructural design for improving the ductility of the initially brittle RHEA. The microstructure of $\text{Al}_{0.5}\text{NbTa}_{0.8}\text{Ti}_{1.5}\text{V}_{0.2}\text{Zr}$ was successfully adjusted by using different heat treatments [60]. Under the as-cast condition (1) the alloy originally showed a basket weave-like continuous B2 as the matrix with discrete bcc phase as precipitates; after quenching from 1400°C followed by 20 minutes of homogenizing treatment, the alloy showed a bcc matrix with nano-scaled B2 precipitates, referred as condition (2); the alloy in condition (2) was further annealed at 600°C for 120 hours and water-quenched to produce a continuous bcc matrix with around 50 nm size of discrete B2 precipitates. Across all three conditions, the chemical composition of the bcc phase is mainly about Nb and Ta and the B2 phase is always Zr and Al (Figure 3.9).

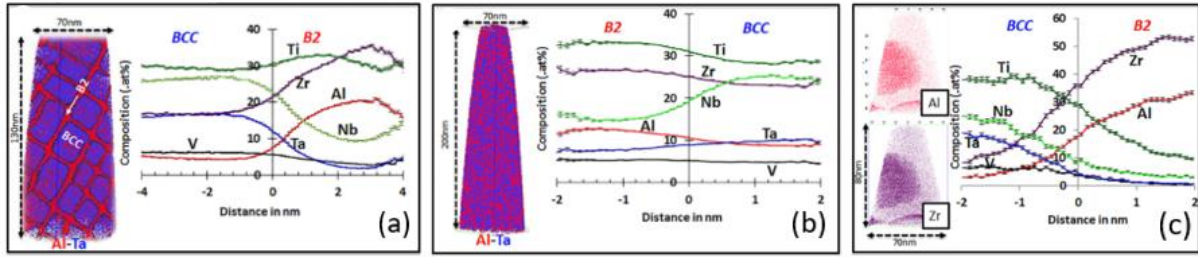


Figure 3.9. APT re-construction of Al-(red) and Ta-(blue) rich regions (left) and compositional changes across a bcc-B2 interface (right) of $\text{Al}_{0.5}\text{NbTa}_{0.8}\text{Ti}_{1.5}\text{V}_{0.2}\text{Zr}$ under condition (1) (a); condition (2) (b); condition (3) (c).

Reproduced from Ref. [60], Open Access (Scientific Reports).

Accordingly, the mechanical properties were changed because of this microstructural reversion. Alloy under condition (1) showed a clear high strength at 25°C and 600°C; condition (2) provided the highest compressive strain; while condition (3) gave a good combination of strength and compressive strain (Figure 3.10). This attempt validated again that the superalloy-like RHEAs are supposed to equip a structure with soft bcc phase as the matrix and hard B2 phase as coherent precipitates.

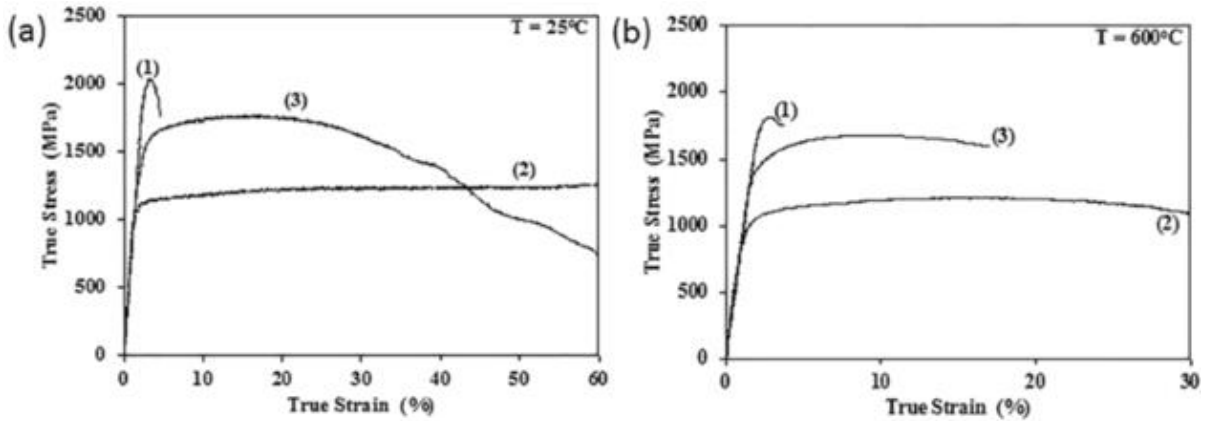


Figure 3.10. Compressive true strain-stress curves of $\text{Al}_{0.5}\text{NbTa}_{0.8}\text{Ti}_{1.5}\text{V}_{0.2}\text{Zr}$ under different conditions (1), (2), (3) after heat treatments at 25°C (a), 600°C (b). Reproduced from Ref. [60], Open Access (Scientific Reports).

Since the matrix and precipitates can be easily reversed by using heat treatments, two points are worth thinking when considering to put refractory high entropy superalloys into potential high temperature applications: phase inversion transformation [64], [65] and thermal stability of phases [66], [67].

Consequently, again the $\text{Al}_{0.5}\text{NbTa}_{0.8}\text{Ti}_{1.5}\text{V}_{0.2}\text{Zr}$ alloy was used for isothermal heat treatments over different time spans [64]. The alloy was first homogenized at 1200°C for 2 hours followed by water quenched and then annealed at 600°C for 0.5, 5, 12, 24, 120 h. Figure 3.11 shows the distribution of Al ions as a traceable element for the transformation of ordered B2 phase during this process. It can be clearly seen that from the start Al is mainly enriched along the channels and then it gradually grows

and gets wider after 5h of exposure. Meanwhile, bulge is starting to form at the intersections of the B2 channel which is visible in Figure 3.11 (c). These bulges grow and lead to thinning at the centers as can be observed after 24h in Figure 3.11 (e) with thinned channels connecting them together. After annealing for 120h, the structure is coarse and only portions of B2 (Al) and bcc (Nb) regions are shown in Figure 3.11 (f). This inversion of bcc and B2 phases stems from the spinodal decomposition mechanism which can be achieved by different heat treatments. There is a strong miscibility gap presented between Ta-Zr, Nb-Zr binary phase diagrams [68], [69]. At high temperatures the bcc phase spinodally decomposes into two bcc phases with different compositional partitions with Nb (Ta) and Zr, and the Zr enriched bcc phase subsequently undergoes chemical ordering transforming into the B2 phase with Al addition due to their big electronegativity difference [64].

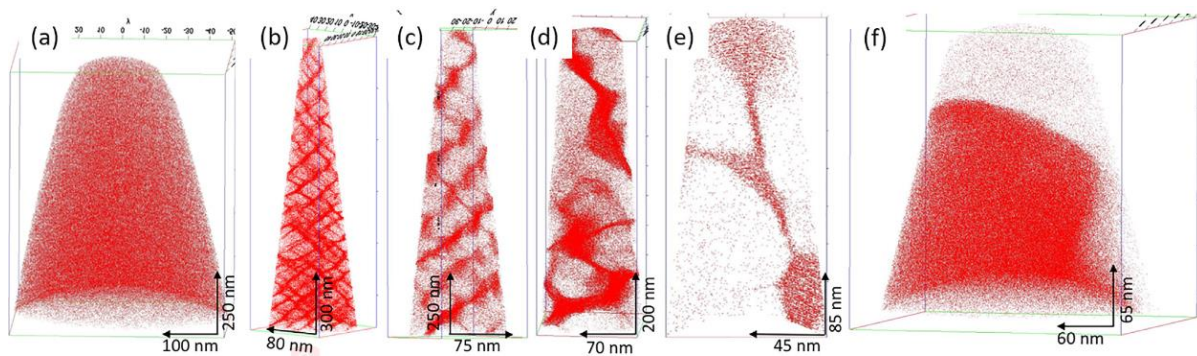


Figure 3.11. APT Al ion maps from the isothermal annealed samples of $\text{Al}_{0.5}\text{NbTa}_{0.8}\text{Ti}_{1.5}\text{V}_{0.2}\text{Zr}$ at $600^\circ\text{C}/x \text{ h}$. $x=(a)$ 0, (b) 0.5, (c) 5, (d) 12, (e) 24 and (f) 120. Reproduced from Ref. [64], with the permission of Elsevier.

Next concern is the thermal stability, which is equally important to microstructural arrangement since the alloys are expected to retain their mechanical properties throughout their lifetime. Homogenized alloys of $\text{AlNbTa}_{0.5}\text{TiZr}_{0.5}$ and $\text{AlMo}_{0.5}\text{NbTa}_{0.5}\text{TiZr}_{0.5}$, both from the AlMoNbTaTiZr system, are chosen to put under 1200°C , 1000°C , and 800°C for 1000h [66]. Results have showed that $\text{AlNbTa}_{0.5}\text{TiZr}_{0.5}$ exposed at 1200°C , 1000°C and 800°C resulted in further intragranular precipitate of the hexagonal Al-Zr intermetallic, the formation of an Al-Nb rich orthorhombic phase and hexagonal Al-Nb-Ti phase in different levels; while the $\text{AlMo}_{0.5}\text{NbTa}_{0.5}\text{TiZr}_{0.5}$ alloy resulted in Al-Zr rich hexagonal intermetallic phase when being exposed at 1200°C and 1000°C , and a desirable fine scale B2-bcc microstructure at 800°C (Figure 3.12). In comparison with two alloys here, a clear beneficial impact from the addition of Mo on the microstructural stability is found below 1000°C , after a long duration of annealing. However, the intragranular precipitation of Al-Zr intermetallic phase remains a great concern as it is likely to be detrimental to alloy properties [66]. Furthermore, the recent work on the effect of Al on the formation and stability of bcc-B2 microstructure from Ti-Ta-Zr- Al_x system was carried out by Whitfield et al. [67], which again is based on the thinking that Al is fundamentally important to the ordering of Zr-rich bcc to B2 at high temperatures. The results further extended and reinforced the previous findings in that

the Al content > 5 at% in bulk is needed for the ordering of Zr rich bcc phase into B2, which happens after the spinodal decomposition; the B2 phase is only stable to relatively moderate temperatures lower than 900°C; and the deleterious intragranular Al-Zr-rich intermetallics were observed following long duration of thermal exposures [67].

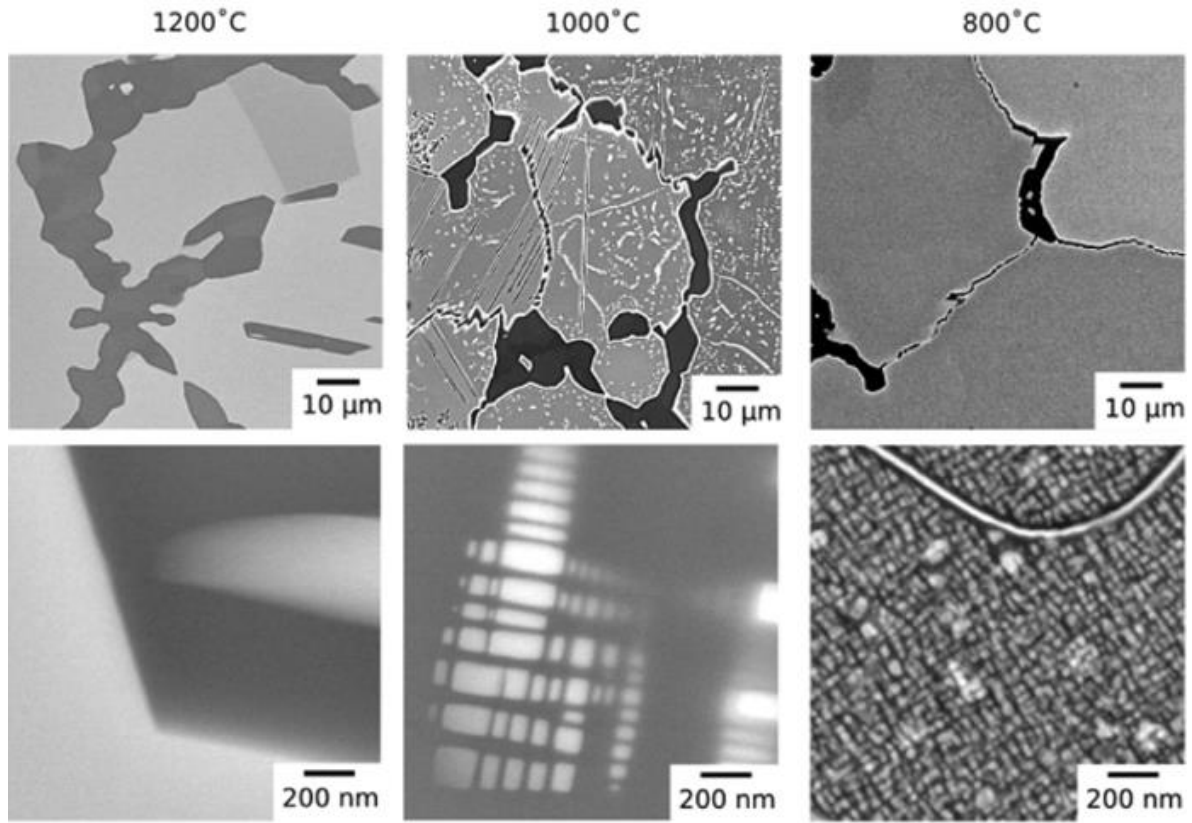


Figure 3.12. BSE images of $\text{AlMo}_{0.5}\text{NbTa}_{0.5}\text{TiZr}_{0.5}$ following 1000h of thermal exposure at 1200°C, 1000°C and 800°C. The magnification of the images increases from top to bottom. Reproduced from Ref. [66], with the permission of Elsevier Science & Technology Journals.

This phases inversion reflects the thermal instability at high temperatures, which is one fatal negative side of this alloy design concept based on spinodal decomposition. Another negative side is about the lattice misfit between these two phases. Lattice misfit parameter is calculated by $\varepsilon = 2 \frac{a_{b2} - a_{bcc}}{a_{b2} + a_{bcc}}$, ~0.1% for spherical precipitation and ~0.5% for cuboidal precipitation to lower the coarsening rate [70]. Misfit of 0.6% was reported for the $\text{Al}_{0.5}\text{NbTa}_{0.8}\text{Ti}_{1.5}\text{V}_{0.2}\text{Zr}$ alloy in the homogenized condition after casting [63], which is already larger than normal Ni-based superalloys presenting the rafting or coarsening of the γ' precipitate [71], [72]. A misfit parameter of 0.3% between γ -matrix and γ' -precipitates for example will expect a lattice misfit stress of 375.9 MPa within the interfaces [73]. The same goes for the modulus misfit between two phases. Commonly an elastically softer phase forms the network and wraps the harder particles. As is well accepted, the coarsening of microstructures strongly depends on the interplay between the interfacial and elastic energies [64]. A minimization of the elastic strain

energy requires that the elastically hard phase deforms less than the soft one. Thus, the elastic energy is less for discrete hard precipitates in a continuous soft matrix than for discrete soft precipitates in a continuous hard matrix [64]. Last but not least, heterointerfaces with complete compositional difference and large misfit will also easily act as the oxygen absorption and transportation path which will further compromise the comprehensive properties of alloys. Exploration and development of stable and coherent precipitates with low misfit for refractory high entropy superalloys at temperatures higher than what conventional Ni-based superalloys achieve, is a rather important and promising scientific topic.

3.2 Ductility at room temperature

Due to the high cost of refractory raw metals and related processing procedures, RHEAs should be considered for application areas with high competitiveness like aerospace or nuclear reactors for example. Although a high yield strength at HT is always a priority for these alloys, a non-zero ductility at RT is also a prerequisite for materials to be processed. Three ductility criteria for single-phase bcc alloys (Figure 3.13) are summarized here [74]: the *Pettifor and Pugh criterion* [75], [76] claimed that materials with non-directional metallic bonds are intrinsically ductile, with a positive Cauchy pressure $C_{12}-C_{44}>0$ and $G/B<0.42$ (G is shear modulus, and B is bulk modulus) [77], [78]; the *valence electron concentration (VEC) criterion* claimed by Sheikh et al.[79] showed that RHEAs made from elements of transition groups 4, 5 and 6 are ductile with a VEC value lower than 4.5; this was suggested to revise by Senkov et al. [74] who recently proposed that the ductile-to-brittle transition instead covers a range of VEC values and RHEAs with a tensile σ_y of ≤ 1200 MPa and compressive σ_y of ≤ 1500 MPa are ductile; the *Rice and Thomson criterion* [80] found that crystals whose dislocations have wide cores and small values of the parameter Gb/γ ($<7.5-10$) are ductile. Currently, there exist quite a few RHEAs with tensile ductility at RT, but the problem is that those alloys with decent yield stress at HT rarely have any tensile elongation at RT; at most they exhibit some plasticity under compression. The defect tolerance capacity of alloys under compression is much higher than that under tension, rendering the compression test less defect sensitive. However, in reality the material is very sensitive to defects which will cause premature failure resulting in catastrophic outcomes. Requiring to have non-zero tensile elongation for RHEAs will benefit their future applications. Below, several potential means to cope with this ductility issue which the RHEAs are facing now are described.

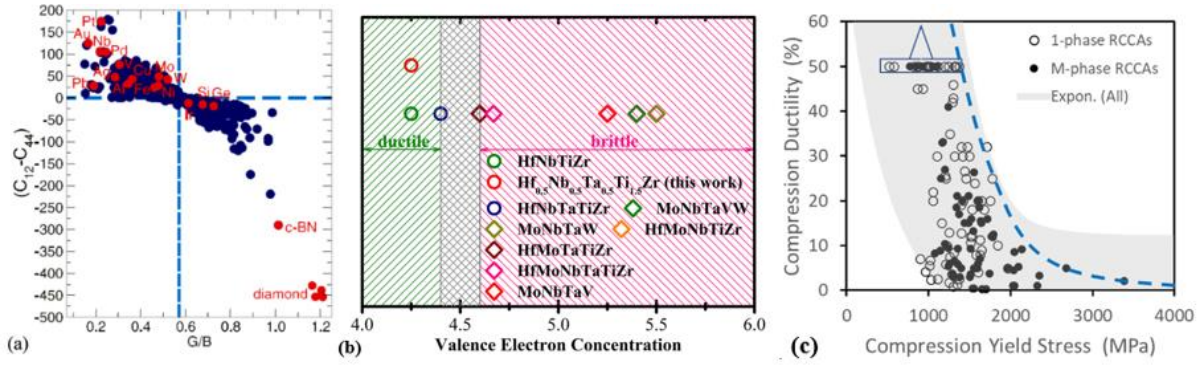


Figure 3.13. (a) Correlation between $(C_{12}-C_{44})$ and G/B . The top left corner with $(C_{12}-C_{44}) > 0$ and $G/B < 0.42$ are ductile. Reproduced from Ref. [60], Open Access (Scientific Reports); (b) alloys with VEC lower than 4.5 are ductile. Reproduced from Ref. [79] with the permission of American Institute of Physics; (c) alloys with compressive yield stress lower than 1500 MPa are ductile. Reproduced from Ref. [74], with the permission of Elsevier Science & Technology Journals.

3.2.1 Valence electron concentration (VEC) engineering

According to the Hume-Rothery rule for solid solution formation, electron concentration is decisive to form different crystal structures [81]. There are basically two definitions of electron concentration: average number of itinerant electrons per atom, e/a , and the number of total electrons including the d -electrons accommodated in the valence band, called valence electron concentration or VEC [82], [83]. VEC for a multi-component alloy can be defined as the weighted average from VEC of the constituent components: $\sum_{i=1}^n C_i(VEC)_i$. C_i is mole fraction and VEC_i is the VEC for the individual element. Based on the results from Ref.[26], the fcc phase are found to be stable at higher VEC (≥ 8) and the bcc phase is stable at lower VEC (≤ 6.87) instead. Further, from 9 RHEAs made from groups 4, 5, 6, Sheikh et al. found that ductile alloys have a $VEC \leq 4.4$ and they designed one alloy composition $Hf_{0.5}Nb_{0.5}Ta_{0.5}Ti_{1.5}Zr$ to successfully prove the concept with a fracture stress of close to 1 GPa and an elongation of near 20% [79]. This is generally one effective way to design ductile RHEAs within groups 4, 5 and 6 [84]. Senkov et al.[74] recently gathered more alloy compositions with different processing conditions, and they stated that tensile ductility can vary from marginally ductile (1.7%, after severe plastic deformation + annealing) to ductile (20%, after cold rolling + annealing) for the same alloy, $HfNbTaTiZr$ ($VEC = 4.4$). Furthermore, alloys such as $MoNbTi$ ($VEC = 5.0$) and $NbTaTi$ ($VEC = 4.67$) are reported to have tensile elongations of 4% and 18.5% (Figure 3.13). This is understandable and reasonable, since the ductile-to-brittle transition temperature of elements within the same group will gradually increase from top to down, meaning a relatively less tendency of ductility but with the same value of VEC in the lower part of the periodic table. So, alloying with W rather than Mo, both having the same VEC, will result in different ductility. In general, alloying with refractory elements to the left side of the periodic table such as Ti, Zr, Hf is more easily to ductilize material, while alloying with those

to the right side such as Cr, Mo, W is more easily to strengthen the materials but with a decreasing ductility.

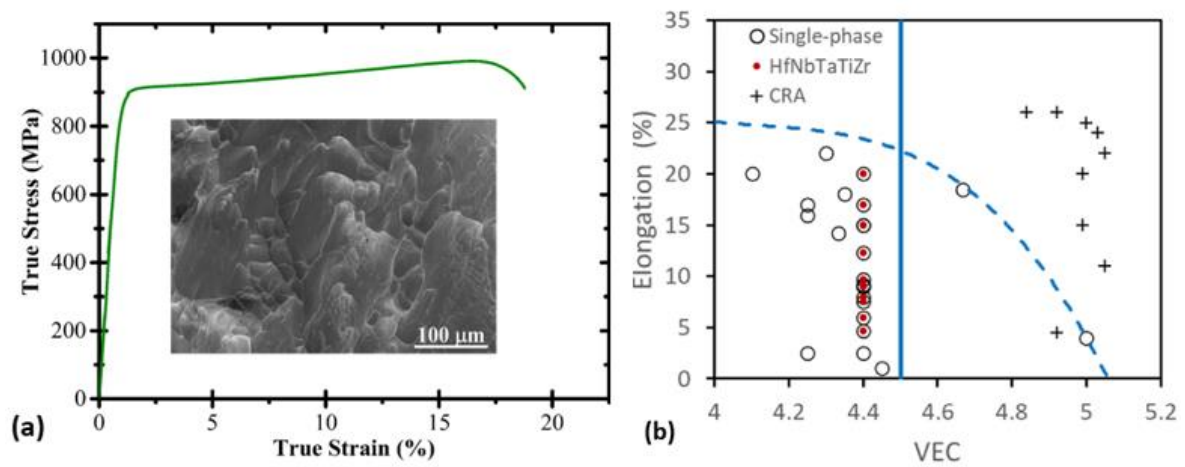


Figure 3.14. (a) True tensile stress-strain curve for as-cast $\text{Hf}_{0.5}\text{Nb}_{0.5}\text{Ta}_{0.5}\text{Ti}_{1.5}\text{Zr}$ as a proof of the VEC concept reproduced from [79] with the permission of American Institute of Physics; (b) VEC vs elongation of RHEAs, in comparison with conventional single-phase bcc refractory alloys (CRA). Reproduced from Ref. [74], with the permission of Elsevier Science & Technology Journals.

3.2.2 Transformation induced plasticity (TRIP)

The energy change of stacking fault can lead to transformation induced twinning or martensitic transformation, improving the strain hardening rate with a further increase of ductility, which is widely used in alloys designed for RT applications such as high strength steels, fcc alloys and titanium alloys. This is also called metastability-engineering to destabilize the master phase during deformation. Employing this strategy to RHEAs developed strain-induced $\text{HfNb}_{0.18}\text{Ta}_{0.18}\text{Ti}_{1.27}\text{Zr}$ alloy [28] and stress-induced Ta_xHfZrTi ($x=1, 0.6, 0.5$, and 0.4) alloys [27]. For the former case, the Ti-enriched alloy, to induce martensitic phase transformation, one can refer to the Bo-Md diagram. For the latter case, the Ta_xHfZrTi alloys, Ti group metals naturally exist in hcp structure in lower temperatures and bcc structure in high temperatures. Lowering the content of Ta, which is bcc structure, will surely increase the tendency for Ti groups metals to dominate the phase structure which are naturally hcp phase at RT. Because Zr, Hf share similar physical and chemical properties with Ti, both metals can be considered as Ti equivalents to some point, which cannot sustain the metastable structures to high temperatures. Obviously, such a combination is not strong enough as well for high temperature applications.

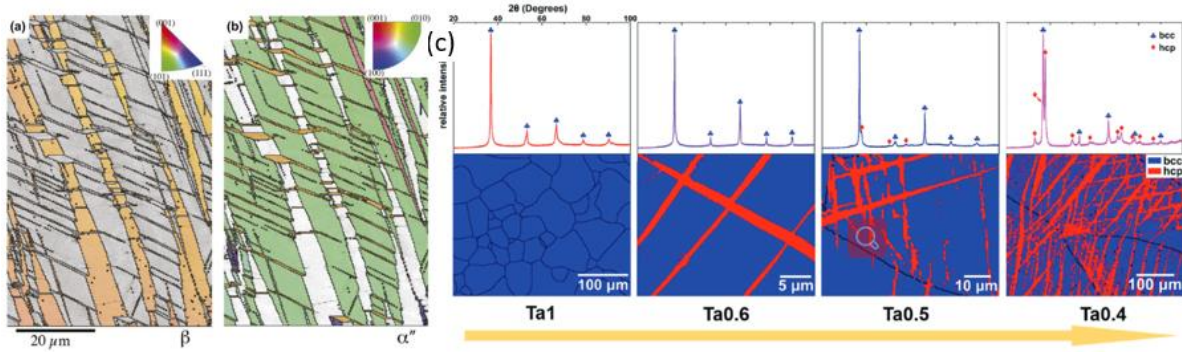


Figure 3.15. (a) Strain-induced formation of the martensitic phase in $\text{HfNb}_{0.18}\text{Ta}_{0.18}\text{Ti}_{1.27}\text{Zr}$, reproduced from Ref. [28], Open Access (Materials Research Letters); (b) Stress-induced formation of the hcp phase in $\text{Ta}_{0.4}\text{HfZrTi}$. Reproduced from Ref. [27], with the permission of John Wiley & Sons – Books.

3.2.3 Solid solution softening (SSS)

While SSH is a common and effective way to strengthen bcc metals and alloys especially at low temperatures, solid solution softening (SSS) can be a way to soften alloys to induce ductility at RT which is most needed for alloys aiming for use at high temperatures. SSS is a well-established phenomenon [85]–[89] starting from the research on iron-based substitutional alloys [90]. It is generally observed in bcc metals at low temperatures as a result of addition of either substitutional or interstitial elements. The amount of interstitial solutes required to produce maximum softening normally ranges from 0.02-0.05 at% [91], much lower than the usual 2-10 at% substitutional solutes required to produce softening under similar test conditions [90].

Before we go to details, let us first revisit the deformation mechanism of bcc structured materials. As mentioned earlier, the deformation of bcc materials is temperature and strain rate dependent, and mainly controlled by the motion of non-planar core of $1/2 \langle 111 \rangle$ screw dislocation. The flow stress is composed of two components: a thermal component called effective stress τ^* and an athermal one, τ_u [92]. The barriers which give rise to the thermal component are of a short-range nature and conversely the barriers which give rise to the athermal component are of a long-range nature. Hence, two of them will have different interaction with dislocations with solute additions [92]. The athermal part, τ_u , as shown below in Figure 3.16 is solely existing at the intermediate temperature range and is almost constant, which makes it basically only affected by the roughness of lattice landscape for dislocations to move across. Only the thermal part τ^* is altered by SSS, with a reduced temperature and strain rate dependence with increasing temperature and strain rate. SSS was once an important research topic with following distinct features [86]:

- 1). Softening predominately affects thermal part τ^* at the low temperature range, below $0.15 T_m$ [92], [93];

- 2). The temperature dependence of the yield stress is relatively large at low temperatures;
- 3). Both interstitial and substitutional solutes can trigger the softening effect;
- 4). Both SSH and SSS could be found in the same alloy system at different temperature ranges: softening at low temperatures while hardening at high temperatures [94].

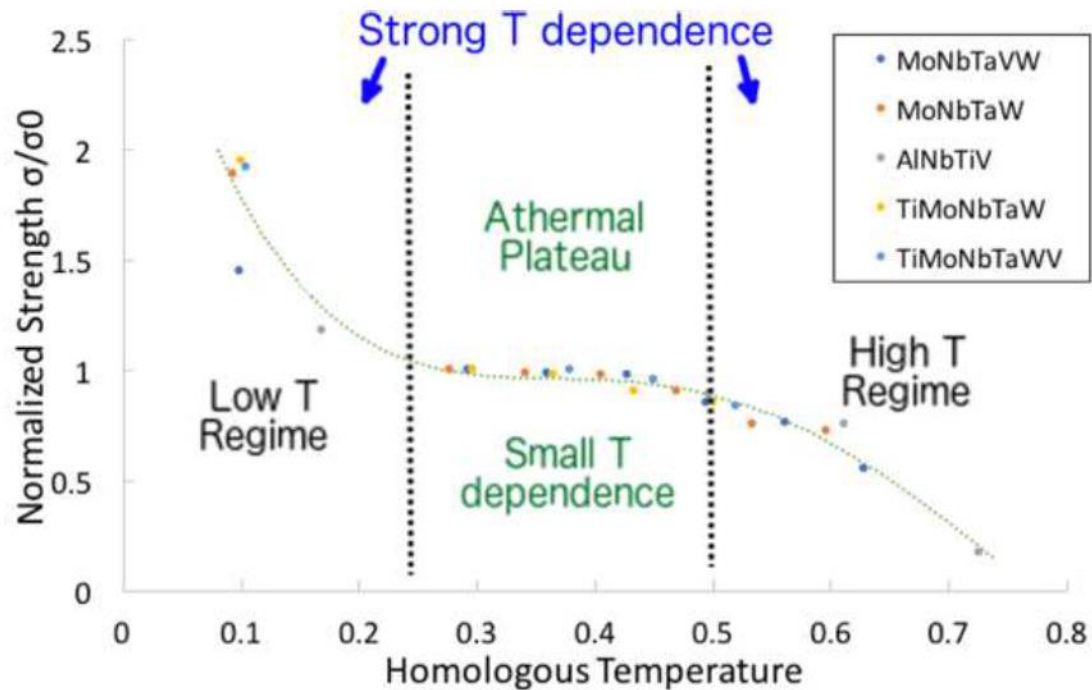


Figure 3.16. Yield stress normalized by the athermal plateau stress and plotted against the respective homologous temperature. Reproduced from Ref. [95], PhD thesis, with the permission of author, F.G. Coury.

There are basically three types of softening mechanism proposed so far, relating to different types of metals, with either intrinsic or extrinsic mechanisms associated with $1/2 \langle 111 \rangle$ screw dislocations mobility controlled by double-kink nucleation and kink migration processes: lowering the Peierls (lattice friction) stress to promote cross slip; electron concentration variation; scavenging of interstitial impurities at very low solute concentration. Kink pairs along a relaxed screw dislocation line is commonly existed in bcc structured materials due to their lowest Gibbs free energy. Under applied external shear stress, the lateral migration of double kink will be activated. With the help of asymmetrical $1/2 \langle 111 \rangle$ screw dislocation core, kinks are also easily formed along intersections of different glide planes which will result in cross-kink glide. When the motions of cross-kink crush into each other, they will finally lead to the formation of jogs to prohibit the further motion of dislocations, thus leading to strengthening. When it comes to the complex multi-element alloys such as RHEAs, the scenario will become even more complicated. In most cases alloys are strengthened without any trace of softening, as the added solutes are already saturated for the double-kink to form, and extra solutes

restrain the further movement of screw dislocations. Therefore, a competition between double kink nucleation and kink migration (Figure 3.17) needs to be deliberately configured to tailor the plasticity behavior of bcc materials.

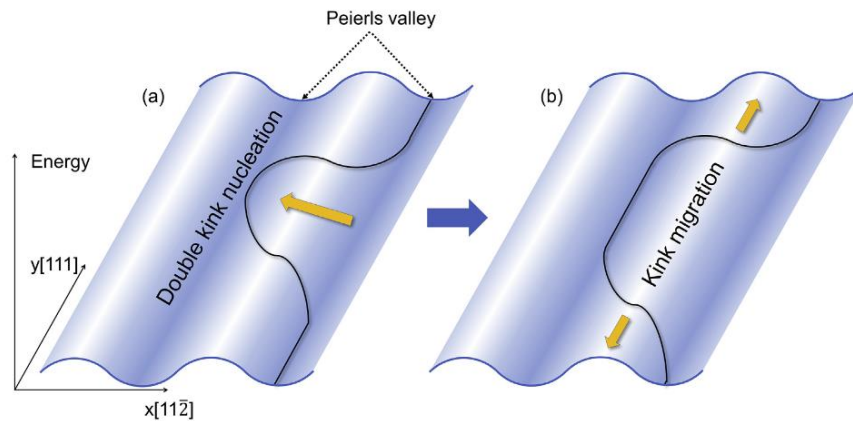


Figure 3.17. Schematic illustration of dislocation motion under the double-kink nucleation and kink migration mechanism in bcc W. (a) Double-kink nucleation: due to the thermal activation, a section of a straight dislocation could bow towards to the adjacent lattice sites to form a double-kink configuration. (b) Kink migration: under the applied stress, the kinks migrate apart along the direction of the dislocation line, which results in the whole dislocation moving to the left adjacent site. Reproduced from Ref. [96], with the permission of Elsevier.

Three types of softening phenomenon mentioned above can be exemplified by three different types of alloys. Firstly, in binary iron alloys [90], the hardness values decrease in most cases with solute concentrations lower than 4 at% at 188 K and 77 K (Figure 3.18a), and the hardness values increase with the decrease of temperature (Figure 3.18b). Only in binary iron alloys with the addition of Zr and Hf, the hardness values always increase which is independent of the change of temperature and solute concentration. With the addition of Nb and Ta less than 0.20 at%, the hardness values in these binary iron alloys are always lower than that of the pure iron when the test temperatures are lower than 411 K (Figure 3.18b). Based on the atomic size difference limit for favorable solid solution formation as suggested by Hume-Rothery [97], alloying elements can be divided into three groups here [90]: first category including Zr and Hf with an atomic size difference larger than 15 %, which does not generate any softening effect; second category including Nb and Ta with an atomic size difference just around 15 % which generates softening at very dilute concentrations followed by rapid hardening; the last category including all the remaining elements with an atomic size difference all notably lower than 15% which are all capable of inducing softening at 77 K over solute concentrations up to 8 at% and a reduction of temperature dependence of hardness. In light of these analysis, the atomic size difference between iron and solute seems to play a dominating role in whether softening or hardening will happen. Basically, the softening and hardening of most alloys agree well with the atomic size difference

rule. Mn might be an exception, since its atomic size is very close to Fe, and Mn softens the iron alloy at lower temperature such as 77 K [98].

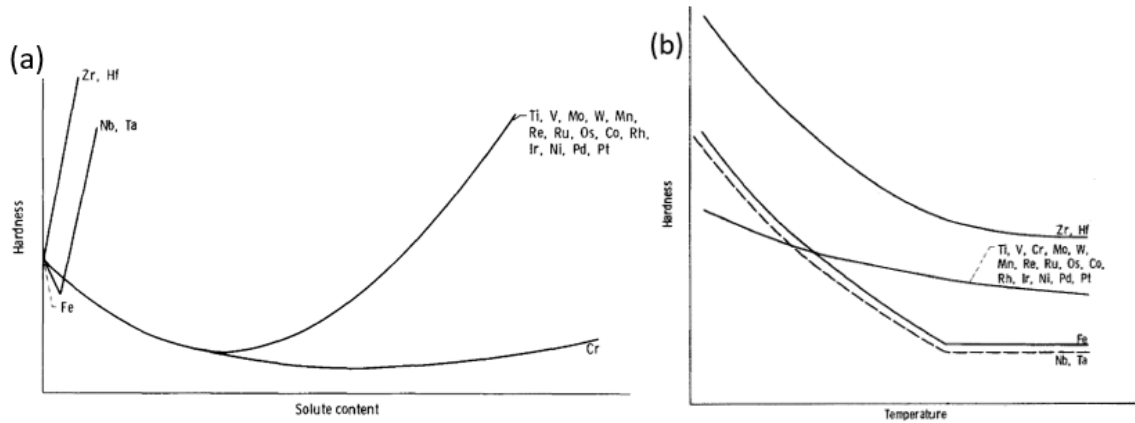


Figure 3.18. (a) Schematic representation of solute effects in binary iron alloys at 77K; (b) temperature dependence of hardness of unalloyed iron and binary iron alloys. Reproduced from Ref. [90], with the permission of Elsevier Science & Technology Journals.

Secondly, softening can be caused by the electron concentration variation, typically in Mo and W. For Mo and W alloys, Pt, Ir, Os and Re solutes lead to softening and the initial softening does not necessarily correlate with atomic radii. Instead, the solute-dislocation interactions, which change the bcc asymmetrical dislocation core structure and elastic stress field around it, are essentially due to the electron concentration variation [88], [94], [96], [99]–[101]. The softening occurs within the solid solution frame, which means this phenomenon can be partially or fully explained by the solid solution model. The model is developed based on thermally activated motion of screw dislocations by double-kink nucleation and kink migration processes when it comes to bcc structured materials. Both processes are rate-limited and one of them dominates at different temperatures. The stress, σ , experimentally measured against applied strain, ε , correlates to these two processes at a constant strain rate $\dot{\varepsilon}$ [102]:

$$\dot{\varepsilon} = 0.94b^2\rho_m * [(\text{nucleation rate})^{-1} + (\text{migration rate})^{-1}]^{-1}$$

where b is the Burgers vector length, ρ_m is the mobile dislocation density per area. Both rates are thermally activated and can be further elaborated by the Arrhenius equation as (attempt frequency) $\times \exp [-(\text{enthalpy barrier})/(k_B T)]$, where k_B is Boltzmann's constant and T is temperature. The enthalpy barrier has a stress scale and an energy scale, and both can be affected by the addition of solutes [102]. The energy scale is connected to the direct solute-dislocation core interaction energy, while the stress scale is correlated to the Peierls misfit (the ability to change stiffness) for moving a single atomic row

in the screw dislocation core. We take the softening effect in Mo alloys here as an example. Re shows a weak, short-range interaction with Mo, but it has a larger Peierls misfit associated with the stress scales than Pt does in this case (Figure 3.19 a1, b1). The weaker interaction and larger Peierls misfit of Re produce a small softening effect; but these effects enhance at high concentrations where multiple solutes interact with dislocations. The large attractive interaction of Pt produces a substantial change in the energy scale and strong initial softening, but quickly leads to hardening at higher concentrations [102]. The predicted strength for Mo-Re and Mo-Pt with changing solute concentration for several temperatures compared with experimental results is shown in Figure 3.19 a2, b2 [102]. The attractive interaction of Re to Mo leads to softening for low solutes because of the increased double-kink nucleation. As the concentration increases, there is a crossover to kink migration dominated flow stress which hardens with additional solutes. The crossover happens at lower concentration for higher temperatures because kink migration becomes more dominated than double-kink nucleation at higher temperatures. The same trend goes for the Mo-Pt case.

The direct solute-induced changes to energy and stress scales of double-kink nucleation and kink migration are sufficient when coupled with correct interaction parameters, to quantitatively interpret experimental observations [102]. The same calculation method has been used for W [96] and other bcc metals [94]. Al and Mn were proposed to be promising substitutes for Re as these two elements could introduce similar softening effects as what Re does in bcc W from simulations [96].

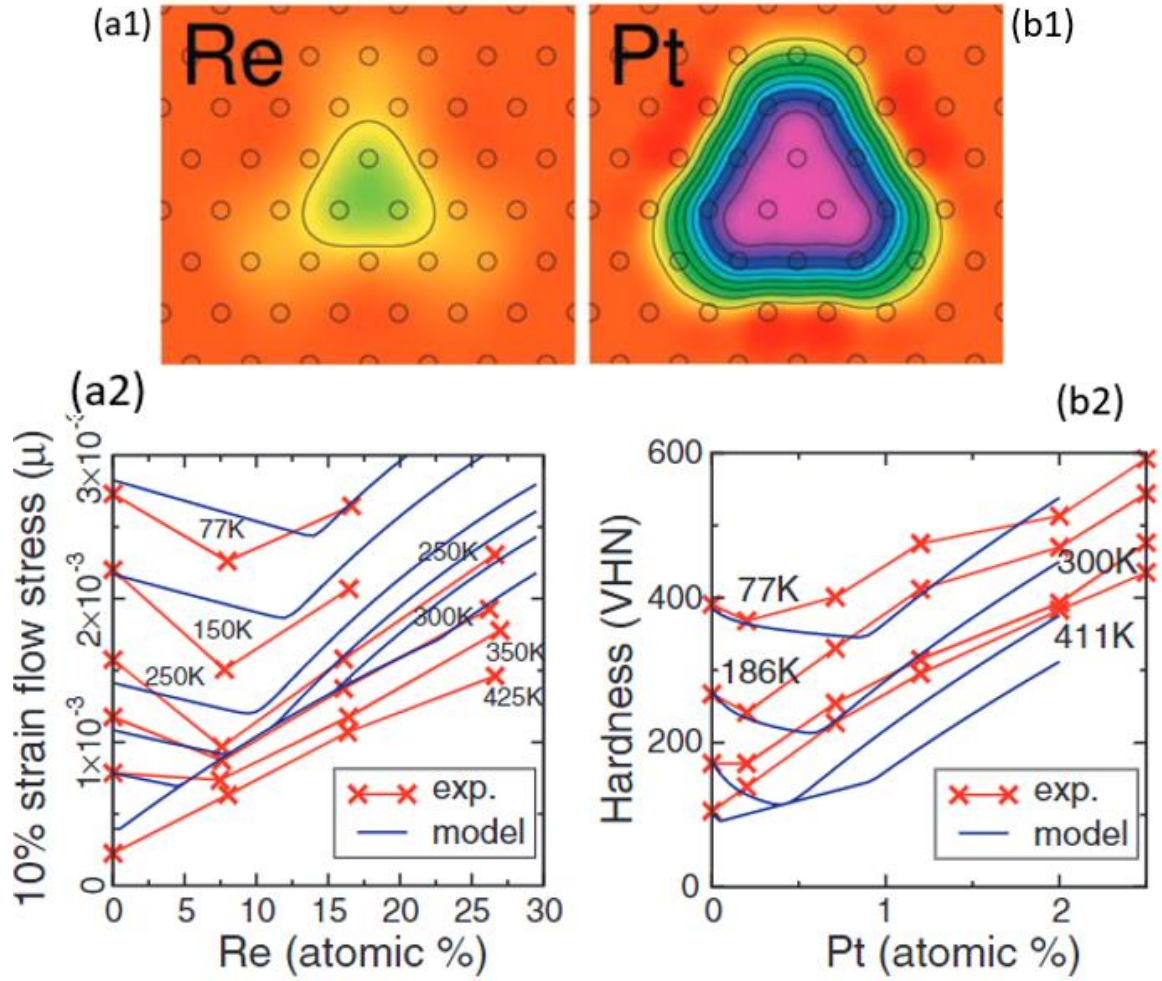


Figure 3.19. Solute-dislocation interaction-energy profile for Re (left) (a1) and Pt (right) (b1) in Mo. The contours are at 0.1-eV intervals, and the interaction is attractive for all sites. Each circle is a possible lattice site for a solute atom in an atomic row; the dislocation is located in the center of the profile. The Pt dislocation interaction is stronger and has a longer range than Re. The interaction energy E_{int} is the maximum value in the profile. Predicted strength for Mo-Re and Mo-Pt are shown as a function of solute concentration for different temperatures, compared with experiments. (a2) Flow stress at 10% strain for Mo-Re and experiments. The flow stress is scaled to the shear modulus $\mu = 139$ GPa. (b2) Vickers hardness number (VHN) for Mo-Pt and experiments. Reproduced from Ref. [102], with the permission of American Association for the Advancement of Science.

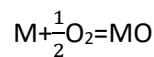
Thirdly, softening can be caused by scavenging of interstitial impurities at very low solute concentrations, typically in Na and Ta. There are studies revealing that the softening effects in Nb and Ta alloys can be eliminated by using high-purity raw metals, which suggests that softening is related to the interstitial impurity [93], [103], [104].

Softening also happen in some iron-based alloys with precipitates [88]. Quenching and micro- and macro-deformation can reduce or prevent softening. The mechanisms involved are still not clear and

they might be different with different materials. In general, SSS is not common in metallic materials, and efforts are desperately needed to dedicate into this research field in the future.

3.3 Oxidation resistance

The oxidation of materials working at high temperatures can cause the degradation and lead to the premature failure, which will be a disaster for materials. Thus, the research on the high temperature oxidation of metals and alloys is important. Materials will react with oxygen differently depending on chemical reaction environment and conditions. For regular oxidation of metallic materials, the major reaction taking place is as follows:



Under different temperatures and pressures, the reaction direction and stability of a system are determined by the Gibbs free energy, G , which is:

$$G = H - TS$$

Where the H is the enthalpy, T is absolute temperature, and S is entropy. The reaction with a direction of lowering the G will be prioritized. Figure 3.20 is the Ellingham diagram displaying the standard free energy G for the formation of different oxides under different partial oxygen pressures and temperatures at the equilibrium state. An obvious tendency is that oxidation reactions will get severe with an increase of temperature. In terms of the three groups of refractory metals, the oxidation under identical conditions is following this sequence: Zr (Hf), Ti, V (Nb, Ta), Cr, Mo (W). Meanwhile, the Pilling–Bedworth ratio [105] for different oxides can be decisive. For instance, ZrO_2 , HfO_2 and TiO_2 with a high Pilling–Bedworth ratio of 1.56, 1.62 and 1.73 will easily be spalled off with a larger volume compared to the substrate metals. As for the stable oxides of V_2O_5 , MoO_3 , WO_3 , they are easy to get evaporated due to their low melting points and boiling points. For the oxides of Nb_2O_5 , Ta_2O_5 , they have an even larger Pilling–Bedworth ratio over 2 and a low melting and boiling points which are the worst for the oxidation protection. Furthermore, their Gibbs free energy of formation of oxides are lower than that of other refractory oxides which will have a selective oxidation prior to the formation of MoO_3 and WO_3 . Thus, there is a consensus that the refractory alloys cannot be successfully used for high temperatures unless some intrinsic oxidation resistance is provided by themselves. Protection coating is an option but still there is a high risk if the coating fails. The research of oxidation resistance performance of refractory materials is of course important.

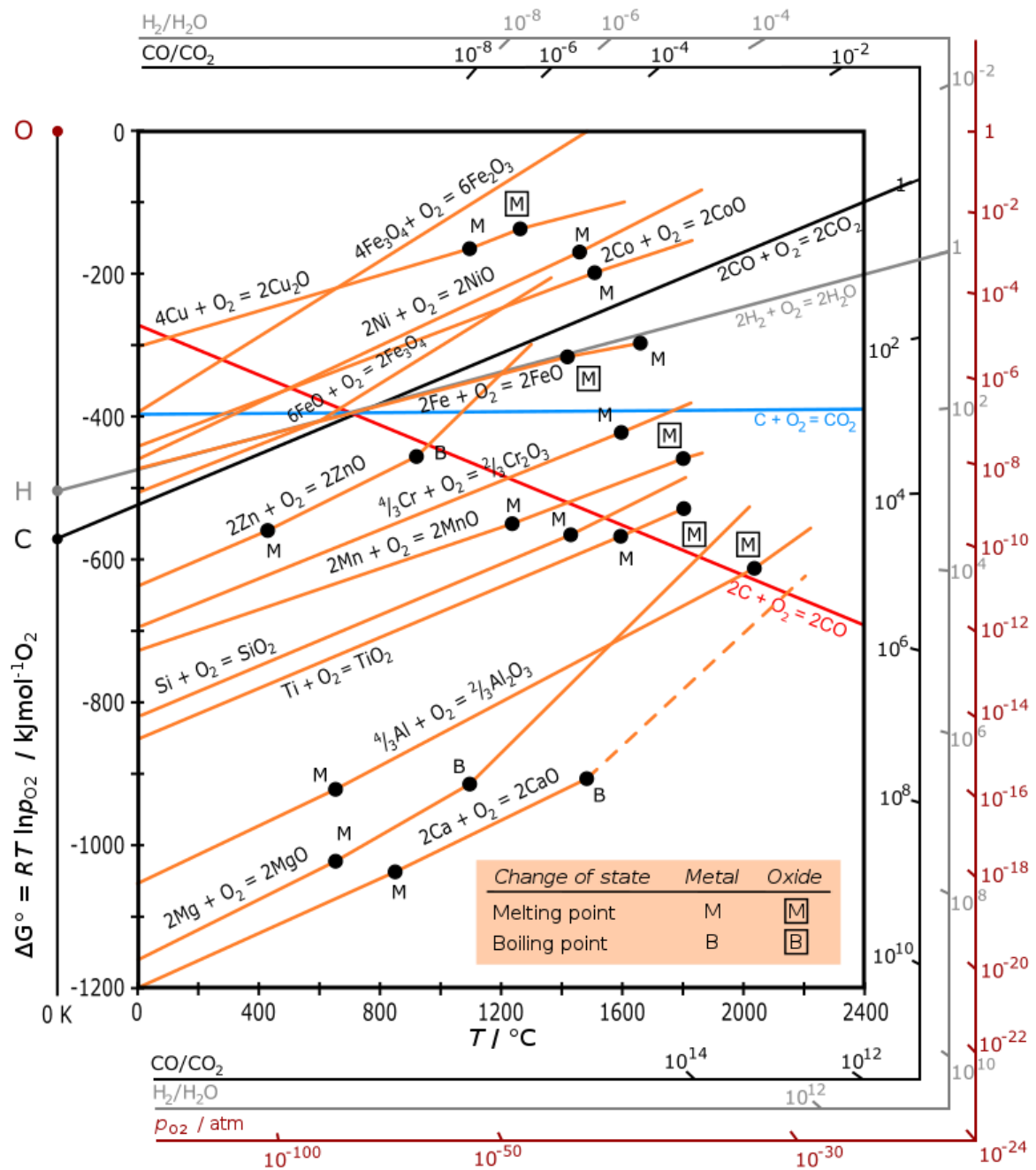


Figure 3.20. Ellingham diagram for several metals giving the free energy of formation of metal oxides and the corresponding oxygen partial pressure at equilibrium [106] (From Wikipedia, under Creative Commons Attribution).

Based on the previous knowledge gained from traditional alloys, one typical way to improve the oxidation resistance of metallic materials is seeking for the formation of oxidation protective layers by alloying elements such as Cr, Al, and Si. Their oxides are oxidation resistant and can be working in certain range of temperatures. Especially, the addition of Cr can have a potent positive effect on the accelerative formation of Al_2O_3 oxide, and these two elements, i.e., Cr and Al, are commonly used

together for the anti-oxidation alloys. The Al_2O_3 layer has high thermal stability and compact rate and can work along a high temperature range up to 1000°C , which is a perfect choice for almost all the anti-oxidation scenarios. Cr_2O_3 is stable working under 1000°C , and higher temperatures would lead to the formation of volatile CrO_3 layer [107]. The Al_2O_3 scale exhibits parabolic growth-rate constants that are an order of magnitude lower than those of the Cr_2O_3 scale [108], [109]. SiO_2 is normally used in Nb and Mo alloys, and it is usually combined with B to increase the fluidity of the self-healing SiO_2 protective layer. SiO_2 can also work at high temperatures up to 1000°C [110]. There are already some trials and errors pursuing the formation of Al- or Cr- related oxides scales. (Ti)AlCrMo-(Ta, Nb) system was extensively researched [111], [112]. Regarding the oxidation research of RHEAs, the content of additions of Cr, Al and Si, usually less than 25 at% in commercially anti-oxidation alloys, also needs to be carefully studied. On the one hand, the alloying elements need to ensure the formation of protective layers; on the other hand, the concentration needs to be controlled to prevent the formation of undesirable intermetallic phases, so to not jeopardize the mechanical performance. Same as the synergistic effect of the simultaneous addition of Cr and Al into traditional alloys, the concentration of Cr and Al simultaneously added into RHEAs should be reduced [113]. Due to the larger atomic size and electronegativity difference between refractory elements and Al, Cr and Si, the balance of forming protective scales and forming intermetallic phases needs to be considered. There is always the presence of intermetallic phases such as C14-type Laves phase ($\text{Cr}_2\text{Ta}/\text{Cr}_2\text{Nb}$), A15 phase ($\text{AlMo}_3/\text{Al}(\text{Mo}, \text{Nb})_3$), and the ordering of A2 to B2. Meanwhile, the complex and protective rutile type oxides (like CrTaO_4 , CrNbO_4) can be formed. The addition of Ti plays a crucial role in that their (CrTaO_4 and CrNbO_4) formation simultaneously decreases the amount of less favorable oxides (Nb_2O_5 , Ta_2O_5) and can suppress the formation of A15 phase to some degree [113]. The discovery of the protective scale CrTaO_4 is highly meaningful [111]. This new strategy to intrinsically protect RHEAs at ultra-high temperatures is applied to the equiatomic high entropy alloy Ta-Mo-Cr-Ti-Al alloy [114]. What we can see from Figure 3.21 below is that the alloy has quite good oxidation resistance at high temperatures and the oxidation kinetic curves is showing the parabolic rate rather than the linear rate.

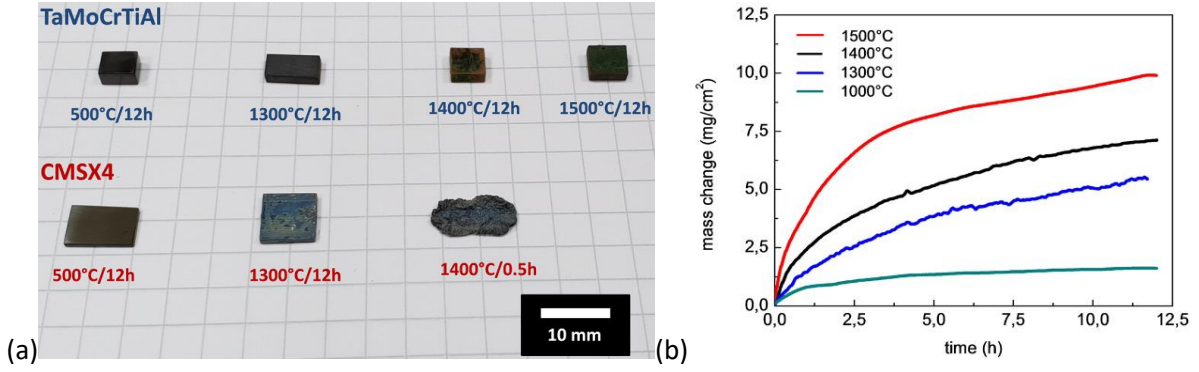


Figure 3.21. (a) Macroscopic micrographs of the alloys oxidized at 500 °C, 1300 °C, 1400 °C and 1500 °C for 12h. (b) The Oxidation curves of the Ta-Mo-Cr-Ti-Al at 1000 °C, 1300 °C, 1400 °C and 1500 °C. Reproduced from Ref. [114], with the permission of Elsevier Science & Technology Journals.

The EDX analysis results from Figure 3.22a [114] on the cross-section of the alloy confirmed the formation of stable CrTaO_4 layer. Additional elements such as Ti and Al are also involved in the formation of this protective oxide. This layer seems to possess highly adhesive properties and suppress the formation of Cr-related intermetallics. The parabolic oxidation constants k_p can be calculated by using the equation listed below:

$$\left(\frac{\Delta m}{A}\right)^2 = k_p * t$$

Figure 3.22b [114] compares the determined parabolic growth rate constants of CrTaO_4 to those of the well-known and widely applied protective oxides as Al_2O_3 , Cr_2O_3 , SiO_2 . The chromia-forming alloys are often used, and their thermal stability is limited to temperatures below 1050°C since at higher temperatures the volatile CrO_3 will form and evaporate leading to a continuous mass loss and unacceptable oxidation rate [115]. Al_2O_3 is stable in a quite wide temperature range and is preferential. The Ni-based superalloys are protected by Al_2O_3 scale. While silica exhibits even lower growth rate at very high temperatures, protective scale only forms above 800°C. At lower temperatures, due to the sluggish diffusion the slow growth rate of SiO_2 prevents the development of a continuous layer resulting in the formation of mixed non-protective oxides [116]. Finally, the growth rate of CrTaO_4 is just only marginally higher than that of Al_2O_3 and lower than that of Cr_2O_3 , which makes this type of protective scale competitive along a wide range of temperatures from 500°C to 1500°C. Apparently, the formation of CrTaO_4 is beneficial and is showing some promise for the intrinsic oxidation resistance of RHEAs.

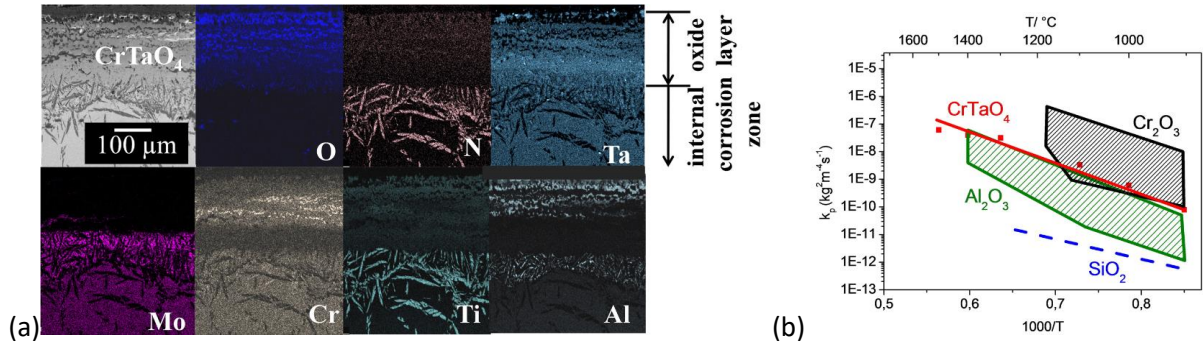


Figure 3.22. (a) Cross-section and EDX analysis of equiatomic Ta-Mo-Cr-Ti-Al alloy after oxidation at 1500 °C for 12h; (b) comparison of the parabolic oxidation constants of CrTaO₄ with those of approved protective oxides Cr₂O₃, SiO₂ and Al₂O₃. Reproduced from Ref. [114], with the permission of Elsevier Science & Technology Journals.

There are some other trials, for example, the addition of Al to form the AlNbO₄ complex oxides [117]–[119]. In summary, the oxidation resistance study and the compositional exploration of RHEAs is of crucial importance and more work surely needs to be done in the future.

4 Experimental method

4.1 Arc-melting

All the alloys studied were prepared by arc-melting equipment supplied by Edmund Bühler GmbH. Melting was carried out through vacuum arc-melting a mixture of different constituent elements with purity higher than 99.9 wt.% in a Ti-gettered high purity argon atmosphere. Different metals were arranged in a way with decreasing melting points from the top to the bottom to minimize the possible evaporation of low melting point elements. The melting and flipping of button ingots by mechanical manipulator were repeated at least five times to insure the chemical homogeneity of the alloy. The arc melter employs a non-consumable tungsten electrode to generate electric arc that heats up the gas and creates plasma. High vacuum is obtained by two-step pumping, firstly using the rotary pump to evacuate the whole system to lower pressure better than 3.0×10^{-3} mbar, then using a diffusion pump to further evacuate the system to a pressure level better than 5.0×10^{-5} mbar. The casting mold, melting plate and crucible are all made from copper and water-cooled by an external chiller to conduct the heat quickly and prevent the overheating of the equipment.



Figure 4.1. Arc melter from Edmund Bühler GmbH.

4.2 Vickers hardness measurement

Hardness quantifies a material's ability to resist plastic deformation from a standard source, normally diamond. Vickers hardness is commonly denoted as HV. With a given load in kilogram-force, an

indentation imprint in square millimeters can be generated. The Vickers hardness can be calculated by the following equation [119], with d being the mean length of diagonals of the indentation imprint.

$$HV \approx 0.1891 \frac{F}{d^2} [\text{N/mm}^2]$$

4.3 Oxidation test

Oxidation tests were carried out in a horizontal ceramic tube furnace that is opened on both ends. During the oxidation experiments, the samples were positioned in the central heating zone using alumina crucible and taken out immediately from the furnace to cool down in air when the experiment was done. The oxidation of alloys was monitored by the weight change per unit area as a function of time and temperature, and also by visual observation.

4.4 High temperature hardness test

Hardness from RT to 1000°C was tested by a high temperature Vickers hardness tester (Intesco-HTM 1400) under high-vacuum, with a load of 1.0 kgf and a dwell time of 10 s. The hardness value was averaged from around 5 indentations at each temperature.

4.5 Universal compression test at room temperature

Cylindrical specimens with a diameter of 6 mm and height of 9 mm were used for all compressive tests. A Zwick Roll Z050 equipment was employed to measure the RT compressive yield stress in laboratory air with an initial strain rate of 0.001/s and a maximum engineering strain around 25% due to the load cell capacity. For each composition, two tests were repeated.

4.6 Gleeble compression test at high temperatures

HT compressive yield stress was measured by Gleeble 3180 under high vacuum ($<4 \times 10^{-1}$ torr) with an initial strain rate of 0.001/s and a target engineering strain of 60%. The heating rate was 10°C/s, 2 minutes of holding time, and cooled by gas. Each composition was tested 3 times per temperature.

4.7 X-ray diffraction

X-ray diffraction was used to determine the crystalline structure. The atoms or molecules of the crystal cause a beam of incident X-rays to diffract along various specific directions, producing secondary waves spreading from electrons. These waves cancel each other in most directions through destructive interference and they only interfere constructively in some directions, determined by the Bragg's law given below, where n is the diffraction order, λ is wavelength of the X-ray source, d is the interplanar distance and 2θ is the diffracted angle [120]. The diffracted planes were then matched to those in standard crystallography databases. In this work, a Bruker AXS D8 X-ray diffractometer (XRD) equipped Cu- K_α radiation was used. The generator was set to 40 kV acceleration voltage and 40mA current.

$$n\lambda = 2d\sin\theta$$

4.8 Scanning electron microscopy

Prior to investigating the microstructure using any electron microscopy, the as-cast alloys were cut by precision saw and then mounted with polyfast by hot mounting method using the Citopress 20 equipment. Mounted samples were then ground by SiC sandpapers attached to a rotating disk. Fine polishing was done using cloth and diamond-paste suspension of 9, 3, 1 μm grit size subsequently. Final polishing was using the 0.05 μm alumina suspension on the same polisher.

For the focused electron beam of SEM, electrons are generated either by field emission gun (FEG) or a source of tungsten or LaB_6 . Generated electrons are accelerated through different size of apertures at a rather high voltage (keV). The beam is then focused by means of various electromagnetic lenses; and scanning coils are used to move the electron beam over the samples surface [121]. Incoming electrons interact with the sample surface, and they are captured by the detector, and later amplified, finally displayed on a TV-screen. The microstructures of RHEAs were studied on the 0.05 μm suspension polished surface using the back-scattering electrons (BSE) mode on a LEO FEG-SEM 1550 equipped with energy dispersive spectrometer (EDS) and electron backscatter diffraction (EBSD).

4.9 Transmission electron microscopy

Transmission electron microscopy (TEM) is a microcopy technique in which a focused beam of electrons from the top transmits through an ultrathin section of specimens to form the images or diffraction patterns depending on the purposes. The electrons generated from a filament or field emission are accelerated by a high voltage above 200kV and they go through different objectives or apertures, and finally transmit through the thin part. The image is then magnified and displayed on an imaging device such as a fluorescent screen. TEM can achieve a significantly high resolution down to atomic level, enabling the nano research on the materials. It can accurately identify different phases of the materials, the elemental distribution at atomic level, and the ways that atoms are arranged.

5 Summary of key results

5.1 Solid solution softening or hardening strategies induced by Minor substitutional addition on soft base refractory alloy --- $\text{Hf}_{20}\text{Nb}_{29.75}\text{Ta}_{29.75}\text{Ti}_{18}\text{-X}_{2.5}$ (X=Mn, Al, Cu, Fe) - (manuscript 1#)

Refractory high entropy alloys with nominal compositions of $\text{Hf}_{20}\text{Nb}_{31}\text{Ta}_{31}\text{Ti}_{18}$ (in at. %, denoted as HNTT) and $\text{Hf}_{20}\text{Nb}_{29.75}\text{Ta}_{29.75}\text{Ti}_{18}\text{-X}_{2.5}$ (X=Mn, Al, Cu, Fe, denoted as HNTT-Mn, HNTT-Al, HNTT-Cu, HNTT-Fe, respectively) were arc-melted using high purity (>99.95%) elements at least 5 times to ensure chemical homogeneity followed by furnace cooling. The nominal content of doped alloying elements was fixed to be 2.5 at.%, to separate the effect of the micro-alloying level on SSH or SSS. Regarding the choice of alloying elements, Mn and Al were selected based on the first-principles calculation results [95], while others were added mainly for the comparison purpose. Directly cast HEAs showed dendritic microstructure enriched with Ta and inter-dendritic microstructure enriched with Ti and Al, from SEM-BSE and EDS results. All tested alloys were identified to be of the single bcc phase which was intended for the purpose of studying SSH or SSS in this work. Vickers hardness for all tested alloys, at temperatures ranging from RT to 1000°C, are given in Table 5.1 and plotted in Figure 5.1. Essentially, all alloys showed a three-stage pattern, reminiscent of how the flow stress varies as a function of temperature in RHEAs and other bcc structured materials [40], [122], [123]. Firstly, at low temperatures below 300°C (400°C for HNTT-Fe), the hardness was strongly influenced by the temperature and different substitutional solutes. Normally, the lower the temperature, the higher the hardness, which was also the scenario seen in this case. With 2.5 at. % nominal addition of Mn, Al, Cu, the HNTT base alloy was softened by 20 %, 18.1 %, 13.3 %, respectively, while 2.5 at. % nominal addition of Fe instead hardened HNTT by 5.2 %. Secondly, at intermediate temperatures ranging from 300°C (400°C for HNTT-Fe) to 800°C, the hardness was almost stabilized, and a plateau was seen. Finally, at high temperatures over 800°C, the hardness of all alloys dropped quickly, presumably due to the increasing impact of thermal diffusion-controlled processes. We will not pay much attention to this high temperature range, since it does not help with the discussion on achieving the decent HT strength. It is noted that at 1000°C the hardness of the HNTT-Fe alloy, with hardness higher than HNTT up to 800°C, was lower than that of HNTT, indicating the loss of SSH at this temperature.

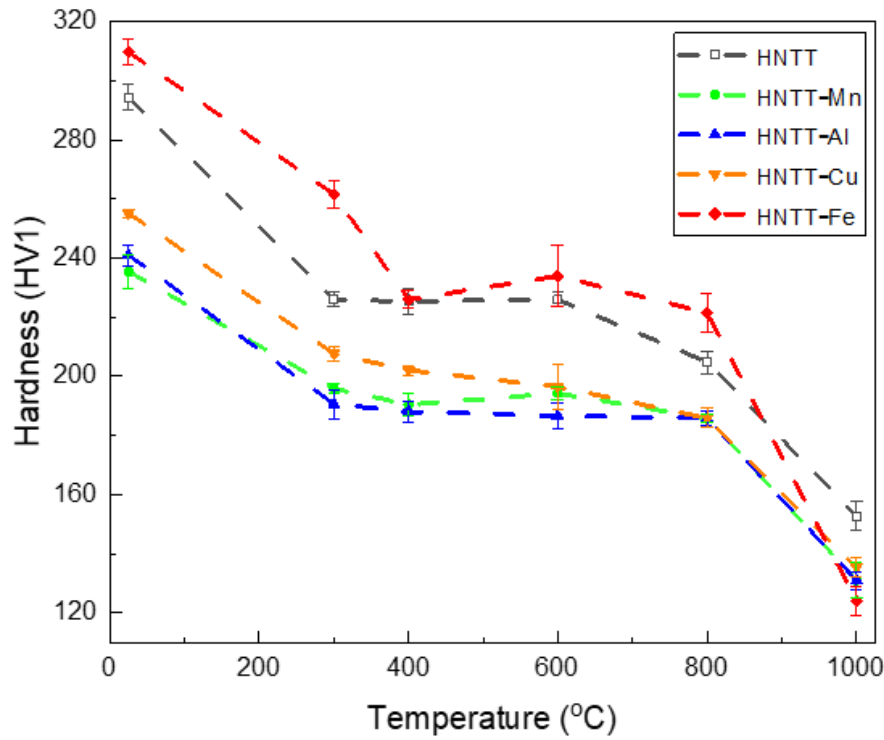


Figure 5.1. Temperature-dependent Vickers hardness for HNTT, HNTT-Mn, HNTT-Al, HNTT-Cu, HNTT-Fe alloys

Table 5.1. Vickers hardness of HNTT, HNTT-Mn, HNTT-Al, HNTT-Cu, HNTT-Fe alloys at various temperatures (in °C)

Alloy ID/Temperature	RT	300	400	600	800	1000
HNTT	294.4±4.5	226.0±2.4	225.4±4.3	226.0±2.5	204.9±3.8	152.7±4.8
HNTT-Mn	235.5±5.8	195.9±1.8	190.5±3.8	194.3±2.2	185.9±1.6	131.0±6.1
HNTT-Al	241.1±3.5	190.7±4.9	188.1±3.7	186.7±4.2	186.0±2.5	130.9±2.9
HNTT-Cu	255.2±1.4	207.7±2.6	202.1±1.7	196.5±7.9	185.9±3.2	135.5±3.3
HNTT-Fe	309.8±4.1	261.6±4.8	226.0±3.1	234.0±10.3	221.6±6.4	124.1±4.9

In summary, minor additions of substitutional elements could cause either solid solution hardening or softening in a $\text{Hf}_{20}\text{Nb}_{31}\text{Ta}_{31}\text{Ti}_{18}$ RHEA, in a wide temperature range. 2.5 at. % nominal addition of Fe led to solid solution hardening due to a kink migration dominated plastic deformation mechanism, while the same nominal content of additions of Mn, Al and Cu caused solid solution softening due to a double-kink nucleation dominated plastic deformation mechanism. A crossover of dominating plastic deformation mechanism from double-kink nucleation to kink migration could be varied by the type and content of solute additions, and the temperature range. On the other hand, for all studied alloys, regardless of the occurrence of solid solution hardening or softening, the hardness variation with temperature showed the same three-stage pattern: a temperature dependent hardness reduction

from room temperature to 300°C/400°C, followed by an athermal plateau from 300°C/400°C to 800°C, influenced mainly by misfits in atomic size and modulus, and finally a quick drop in hardness above 800°C due to the enhanced diffusion-controlled processes.

5.2 Solid solution softening at room temperature and hardening at elevated temperatures simultaneously induced by minor substitutional alloying: A case by minor Mn addition in a $(\text{TiHfNb})_{85}\text{Mo}_{15}$ refractory high entropy alloy - (manuscript 2#)

Based on experimental results we obtained from manuscript 1#, Mn, Al and Cu were identified as effective SSS enabling elements at RT in single-phase bcc structured RHEAs. With an increasing solute concentration of Mn, Al and Cu, the change of Vickers hardness (HV5) of a RT brittle $(\text{TiHfNb})_{85}\text{Mo}_{15}$ alloy was plotted in Figure 5.2. A clear tendency of significant drop of hardness was observed with the minor addition of solutes less than 0.4 at %, particular with Mn. The seemingly slight increase of hardness of the alloy with a nominal 0.1 at % addition of Mn was within the uncertainty range. In this case, Mn as the most promising SSS enabling element was chosen to apply to this RT brittle base alloy, to demonstrate the strategy employing solid solution softening (SSS) at RT and solid solution hardening (SSH) at elevated temperatures, in order to reduce the temperature dependence of yield stress and to achieve a better balance of strength and ductility in single-phase bcc-structured alloys in a wide temperature range.

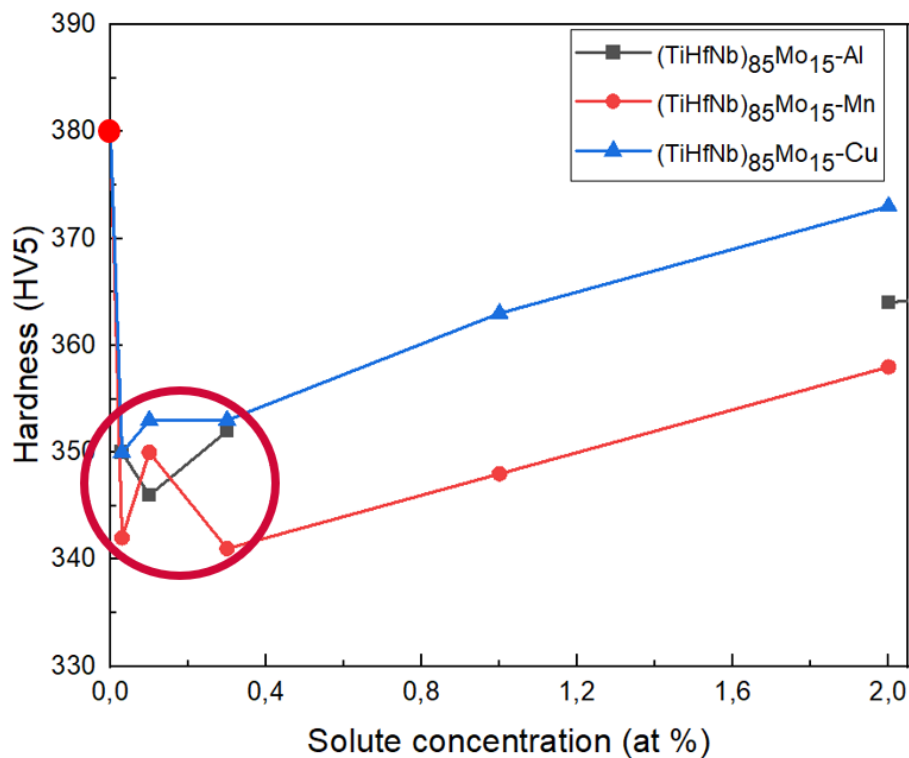


Figure 5.2. Vickers hardness for $(\text{TiHfNb})_{85}\text{Mo}_{15}$ alloys with increasing solute concentrations of Mn, Al and Cu at room temperature

RHEAs with nominal compositions of $(\text{TiHfNb})_{85-x}\text{Mo}_{15}\text{Mn}_x$ ($x=2, 1, 0.3, 0.1, 0.03, 0$, in at%, with alloys denoted as Mn2, Mn1, Mn0.3, Mn0.1, Mn0.03, the base alloy, respectively) were produced by arc melting of high purity (>99.95%) elements at least 5 times to ensure chemical homogeneity followed by natural cooling. Dendritic microstructure enriched with Mo and Nb, and inter-dendritic microstructure enriched with Hf and Ti, were seen in directly cast HEAs by SEM-BSE and EDS. All tested alloys were identified to be of the single bcc phase. Compressive true stress at (a) 25°C, (b) 400°C, (c) 600°C, (d) 800°C, (e) 1000°C for Mn2, Mn1, Mn0.3, Mn0.1, Mn0.03 and the base alloy are summarized in Table 5.2. The temperature dependence of compressive yield stress across all studied alloys from 25°C to 1000°C for all tested alloys are plotted in Figure 5.3.

The yield stress of the base alloy was higher than those alloys with minor Mn additions, thus showing a SSS effect at RT. To be specific, nominal additions of 2%, 1%, 0.3%, 0.1%, 0.03% of Mn softened the base alloy by 2.0%, 4.4%, 9.5%, 6.8%, 6.7%, respectively, in terms of yield stress, which was 5.8%, 8.4%, 10.3%, 7.9%, 10.0% respectively, in terms of Vickers hardness. The softening was most significant at nominal addition of 0.3% Mn. Seen from Fig 5.3 below, at the temperature range from RT to 400°C, the yield stress showed a strong temperature dependence. At the intermediate temperature range, from 400°C to 800°C in this case, the yield stress was almost stabilized. Also, the yield stress of the base alloy was lower than those with minor Mn additions, thus displaying a SSH effect. Taking the yield stresses measured at 600°C as an example, the nominal addition of 2%, 1%, 0.3%, 0.1%, 0.03% of Mn hardened the base alloy by 7.4%, 6.1%, 3.8%, 3.2%, 0.9%, respectively. The hardening level decreased with decreasing Mn content. At high temperatures, 1000°C in this case, the yield stress experienced a quick drop regardless of the amount of Mn additions, due to a typical softening mechanism associated with the activation of thermal diffusional processes and the low melting point of Mn thus its fast diffusion. The plastic deformation at this high temperature range is more studied for time-dependent mechanical properties such as creep and fatigue, which is beyond the scope of the current work.

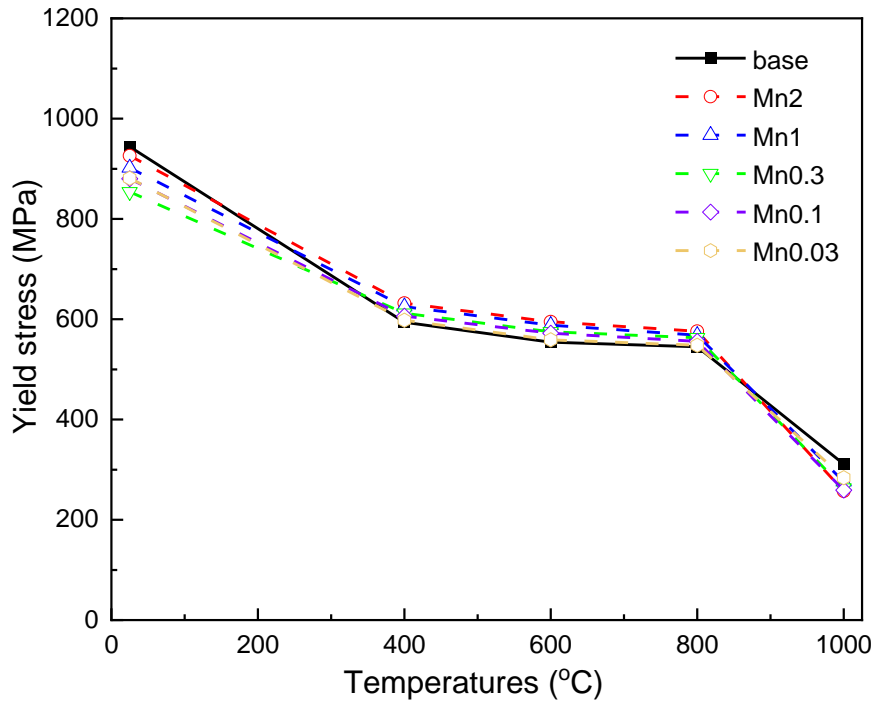


Figure 5.3. Temperature dependence of compressive yield stress across all studied alloys from 25°C to 1000°C.

Table 5.2. Compressive yield stress (σ_y) of studied alloys in as-cast condition from 25°C to 1000°C.

Alloy ID /Temperatures(°C)	Mo15	Mn2	Mn1	Mn0.3	Mn0.1	Mn0.03
25°C ¹	944	926	902	854	880	881
400°C ²	594	632	625	612	606	598
600°C ²	554	595	588	575	572	559
800°C ²	545	576	568	563	556	548
1000°C ²	311	257	276	263	259	254

1: tested using the universal compressive machine; 2: tested using the Gleeble system.

In summary, better balanced strength from low temperatures to intermediate temperatures in a $(\text{TiHfNb})_{85}\text{Mo}_{15}$ RHEA was experimentally achieved here by less than 2 at. % nominal substitutional additions of Mn, combining strategies of SSS at low temperatures and SSH at intermediate temperatures. The yield stress of all studied alloys showed a three-stage pattern: a temperature dependent state at low temperatures governed by SSS, an athermal stage at intermediate temperatures controlled by SSH, and another temperature dependent stage at high temperatures influenced by enhanced thermal diffusional processes. The alloy with 0.3 at. % Mn addition showed

the largest softening effect by 9.5% at RT. The same alloy also exhibited the lowest temperature dependence descriptor $\lambda_{\sigma-T}$ among all studied alloys, indicating the lowest temperature dependence of yield stress before reaching the high temperature range. Overall, SSS at low temperatures holds the potential to induce non-zero tensile ductility for those RHEAs with decent HT strength, which would alleviate the manufacturing and processing concerns, while a simultaneous improvement of yield stress at intermediate temperatures by SSH is important for their applications at elevated temperatures.

6 Conclusions and future prospects

The core idea of the work is to combine solid solution hardening at HT (Target No.1, for HT strength) and solid solution softening at RT (Target No.2, for RT ductility), by minor substitutional additions in selected RHEAs. Our results showed some promise to develop high-performance RHEAs with a better-balanced strength and ductility from low temperatures to intermediate temperatures. We essentially showed two demonstrations of this strategy, and the key results are as follows:

1. The Vicker hardnesses (HV1) of $\text{Hf}_{20}\text{Nb}_{29.75}\text{Ta}_{29.75}\text{Ti}_{18}\text{-X}_{2.5}$ (in at.%, X=Mn, Al, Cu, Fe) alloys showed a three-stage pattern in the temperature range from 25°C to 1000°C: from 25°C to 400°C, a temperature dependent hardness reduction; from 400°C to 800°C, an athermal plateau; and above 800°C, the hardness dropped quickly. The 2.5 at.% nominal addition of Mn, Al and Cu softened the RT ductile base alloy $\text{Hf}_{20}\text{Nb}_{31}\text{Ta}_{31}\text{Ti}_{18}$, while the same amount of Fe hardened the base alloy even straightly, from RT to 800°C;
2. The compressive yield stress of $(\text{TiHfNb})_{85-x}\text{Mo}_{15}\text{Mn}_x$ (in at.%, $x=0.03\sim 2$) alloys also showed a three-stage pattern from 25°C to 1000°C, resembling that of $\text{Hf}_{20}\text{Nb}_{29.75}\text{Ta}_{29.75}\text{Ti}_{18}\text{-X}_{2.5}$ alloys seen in manuscript 1#: a temperature dependent stresses at the low temperature range, followed by an athermal plateau at intermediate temperatures, finally a quick drop at high temperatures. The addition of less than 2 at. % nominal Mn rendered the base alloy $(\text{HfNbTi})_{85}\text{Mo}_{15}$ a reduced yield stress at RT, displaying the softening effect, together with a slightly increased yield stress from 400°C to 800°C, thus showing the hardening effect.

Apparently, there is still a long way to go before RHEAs can be applied as high-temperature structural materials in practice. Next step is to reveal the mechanisms behind this SSS effect at RT, and to mechanistically establish ways to induce non-zero tensile ductility for those RHEAs with decent HT strength, which would alleviate the manufacturing and processing concerns. Simultaneously, we will work on improvement of yield stress at intermediate temperatures by SSH, which is important for their applications at elevated temperatures.

7 Acknowledgements

The work presented in this thesis was carried out under the financial support from the Swedish Research Council (grant number 2019-03559), which is greatly acknowledged. I would like also thank the financial support from the Axel Hultgrens Fund, the JSPS (Japan Society for the Promotion of Science) Summer Program.

The major gratitude goes to my supervisor Sheng Guo, who has been supporting my research throughout the work, both financially and personally. He is not just simply my supervisor, but also my best friend. I also would like to express my gratitude to my assistant supervisor, Dr. Huahai Mao, who helped us with thermodynamics calculations whenever we needed them. Again, as one of my best friends, I hereby thank you so much for your support and considerations. Great thanks to Uta Klement as well, for her support not just as my examiner, but also giving me the timely help anytime when I turned to her.

I am so grateful for the help I got from Yiming Yao. She guided me and assisted me so professionally for using various metallography and characterization equipment, step by step, including but certainly not limited to microscopy. Sincere appreciation also goes to Eric Tam and Roger Sagdahl.

Thanks to my friends and colleagues at Department of Industrial and Materials Science, Chalmers, for their support and creating a friendly working environment.

I would like to thank Prof. Yoko-Yamabe-Mitarai at University of Tokyo, and Prof. Nobuhiro Tsuji at Kyoto University for the useful suggestions and discussions.

Deepest gratitude to my parents, my elder sister and her family for their endless love and unwavering support.

Xiaolong Li

8 References

- [1] P. John. H, 'The hotter the engine, the better', *Science*, vol. 326, no. 5956. pp. 1068–1069.
- [2] J. A. Lemberg and R. O. Ritchie, 'Mo-Si-B alloys for ultrahigh-temperature structural applications', *Advanced Materials*, vol. 24, no. 26, pp. 3445–3480, Jul. 2012.
- [3] R. A. Perkins and G. H. Meier, 'The oxidation behavior and protection of niobium', *JOM*, vol. 42, no. 8, pp. 17–21, 1990.
- [4] O. N. Senkov, G. B. Wilks, D. B. Miracle, C. P. Chuang, and P. K. Liaw, 'Refractory high-entropy alloys', *Intermetallics*, vol. 18, no. 9, pp. 1758–1765, Sep. 2010.
- [5] M. C. Gao, J.-W. Yeh, P. K. Liaw, and Y. Zhang, 'High-Entropy Alloys'.
- [6] Y. F. Ye, Q. Wang, J. Lu, C. T. Liu, and Y. Yang, 'High-entropy alloy: challenges and prospects', *Materials Today*, vol. 19, no. 6, pp. 349–362, Jul. 2016.
- [7] J. W. Yeh *et al.*, 'Nanostructured High-Entropy Alloys with Multiple Principal Elements: Novel Alloy Design Concepts and Outcomes', *Adv Eng Mater*, vol. 6, no. 5, pp. 299–303, May 2004.
- [8] C. Ng, S. Guo, J. Luan, S. Shi, and C. T. Liu, 'Entropy-driven phase stability and slow diffusion kinetics in an Al_{0.5}CoCrCuFeNi high entropy alloy', *Intermetallics*, vol. 31, pp. 165–172, Dec. 2012.
- [9] S. Guo and C. T. Liu, 'Phase stability in high entropy alloys: Formation of solid-solution phase or amorphous phase', *Progress in Natural Science: Materials International*, vol. 21, no. 6, pp. 433–446, Dec. 2011.
- [10] Y. Zhang *et al.*, 'Microstructures and properties of high-entropy alloys', *Prog Mater Sci*, vol. 61, pp. 1–93, Apr. 2014.
- [11] D. B. Miracle and O. N. Senkov, 'A critical review of high entropy alloys and related concepts', *Acta Mater*, vol. 122, pp. 448–511, Jan. 2017.
- [12] S. Guo, Q. Hu, C. Ng, and C. T. Liu, 'More than entropy in high-entropy alloys: Forming solid solutions or amorphous phase', *Intermetallics*, vol. 41, pp. 96–103, 2013.
- [13] Y. Zhang *et al.*, 'Microstructures and properties of high-entropy alloys', *Prog Mater Sci*, vol. 61, pp. 1–93, Apr. 2014.
- [14] B. Cantor, I. T. H. Chang, P. Knight, and A. J. B. Vincent, 'Microstructural development in equiatomic multicomponent alloys', *Materials Science and Engineering: A*, vol. 375–377, no. 1-2 SPEC. ISS., pp. 213–218, Jul. 2004.
- [15] O. N. Senkov, G. B. Wilks, J. M. Scott, and D. B. Miracle, 'Mechanical properties of Nb₂₅Mo₂₅Ta₂₅W₂₅ and V₂₀Nb₂₀Mo₂₀Ta₂₀W₂₀ refractory high entropy alloys', *Intermetallics*, vol. 19, no. 5, pp. 698–706, May 2011.
- [16] O. N. Senkov, J. M. Scott, S. v. Senkova, D. B. Miracle, and C. F. Woodward, 'Microstructure and room temperature properties of a high-entropy TaNbHfZrTi alloy', *J Alloys Compd*, vol. 509, no. 20, pp. 6043–6048, May 2011.

- [17] M. C. Gao, B. Zhang, S. M. Guo, J. W. Qiao, and J. A. Hawk, 'High-Entropy Alloys in Hexagonal Close-Packed Structure', *Metall Mater Trans A Phys Metall Mater Sci*, vol. 47, no. 7, pp. 3322–3332, Jul. 2016.
- [18] M. Vaidya, K. G. Pradeep, B. S. Murty, G. Wilde, S. V. Divinski, 'Bulk tracer diffusion in CoCrFeNi and CoCrFeMnNi high entropy alloys', *Acta Mater*, vol. 146, pp. 211–224, Mar. 2018.
- [19] W. Dong *et al.*, 'Applications of High-Pressure Technology for High-Entropy Alloys: A Review', *Metals* 2019, Vol. 9, Page 867, vol. 9, no. 8, p. 867, Aug. 2019.
- [20] D. B. Miracle and O. N. Senkov, 'A critical review of high entropy alloys and related concepts', *Acta Mater*, vol. 122, pp. 448–511, Jan. 2017.
- [21] F. G. Coury, M. Kaufman, and A. J. Clarke, 'Solid-solution strengthening in refractory high entropy alloys', *Acta Mater*, vol. 175, pp. 66–81, Aug. 2019.
- [22] R. Feng *et al.*, 'Superior High-Temperature Strength in a Supersaturated Refractory High-Entropy Alloy', *Advanced Materials*, 2021.
- [23] O. N. Senkov, T. I. Daboiku, T. M. Butler, M. S. Titus, N. R. Philips, and E. J. Payton, 'High-temperature mechanical properties and oxidation behavior of Hf-27Ta and Hf-21Ta-21X (X is Nb, Mo or W) alloys', *Int J Refract Metals Hard Mater*, vol. 96, Apr. 2021.
- [24] B. Kang, T. Kong, H. J. Ryu, and S. H. Hong, 'Superior mechanical properties and strengthening mechanisms of lightweight AlxCrNbVMo refractory high-entropy alloys (x = 0, 0.5, 1.0) fabricated by the powder metallurgy process', *J Mater Sci Technol*, vol. 69, pp. 32–41, Apr. 2021.
- [25] S. Sheikh, S. Shafeie, and Q. Hu, 'Alloy design for intrinsically ductile refractory high-entropy alloys ARTICLES YOU MAY BE INTERESTED IN', *J. Appl. Phys*, vol. 120, p. 164902, 2016.
- [26] S. Guo, C. Ng, J. Lu, and C. T. Liu, 'Effect of valence electron concentration on stability of fcc or bcc phase in high entropy alloys', *J Appl Phys*, vol. 109, no. 10, p. 103505, May 2011.
- [27] H. Huang *et al.*, 'Phase-Transformation Ductilization of Brittle High-Entropy Alloys via Metastability Engineering', *Adv. Mater*, vol. 29, p. 1701678, 2017.
- [28] L. Liliensten *et al.*, 'Design and tensile properties of a bcc Ti-rich high-entropy alloy with transformation-induced plasticity', *Mater Res Lett*, vol. 5, no. 2, pp. 110–116, Mar. 2017.
- [29] B. Gorr *et al.*, 'High-Temperature Oxidation Behavior of Refractory High-Entropy Alloys: Effect of Alloy Composition', *Oxidation of Metals*, vol. 88, no. 3–4, pp. 339–349, Oct. 2017.
- [30] F. Müller *et al.*, 'On the oxidation mechanism of refractory high entropy alloys', *Corros Sci*, vol. 159, p. 108161, Oct. 201.
- [31] B. Gorr, S. Schellert, F. Müller, H.-J. Christ, A. Kauffmann, and M. Heilmaier, 'Current Status of Research on the Oxidation Behavior of Refractory High Entropy Alloys', 2021.
- [32] S. Suzuki, H. Matsui, and H. Kimura, 'The effect of heat treatment on the grain boundary fracture of recrystallized molybdenum', *Materials Science and Engineering*, vol. 47, no. 3, pp. 209–216, Mar. 1981.
- [33] J. Wadsworth, C. M. Packer, P. M. Chewey, and W. C. Coons, 'A microstructural investigation of the origin of brittle behavior in the transverse direction in Mo-based alloy bars', *Metallurgical Transactions A* 1984 15:9, vol. 15, no. 9, pp. 1741–1752, Sep. 1984.

- [34] J. Wadsworth, T. G. Nieh, and J. J. Stephens, 'Recent advances in aerospace refractory metal alloys', vol. 33, no. 1, pp. 131–150, Jan. 2013.
- [35] O. N. Senkov, D. B. Miracle, K. J. Chaput, and J. P. Couzinie, 'Development and exploration of refractory high entropy alloys—A review', *J Mater Res*, vol. 33, no. 19, pp. 3092–3128, Oct. 2018.
- [36] O. N. Senkov, S. Gorsse, and D. B. Miracle, 'High temperature strength of refractory complex concentrated alloys', *Acta Mater*, vol. 175, pp. 394–405, Aug. 2019.
- [37] F. Maresca and W. A. Curtin, 'Theory of screw dislocation strengthening in random BCC alloys from dilute to "High-Entropy" alloys', *Acta Mater*, vol. 182, pp. 144–162, Jan. 2020.
- [38] A. Ghafarollahi and W. A. Curtin, 'Theory of kink migration in dilute BCC alloys', *Acta Mater*, vol. 215, p. 117078, Aug. 2021.
- [39] C. Lee *et al.*, 'Strength can be controlled by edge dislocations in refractory high-entropy alloys', *Nat Commun*, vol. 12, no. 1, Dec. 2021.
- [40] S. I. Rao, C. Woodward, B. Akdim, O. N. Senkov, and D. Miracle, 'Theory of solid solution strengthening of BCC Chemically Complex Alloys', *Acta Mater*, vol. 209, May 2021.
- [41] S. Laube *et al.*, 'Controlling crystallographic ordering in Mo–Cr–Ti–Al high entropy alloys to enhance ductility', *J Alloys Compd*, vol. 823, May 2020.
- [42] J. P. Couzinié and G. Dirras, 'Body-centered cubic high-entropy alloys: From processing to underlying deformation mechanisms', *Mater Charact*, vol. 147, pp. 533–544, Jan. 2019.
- [43] S. I. Rao *et al.*, 'Atomistic simulations of dislocations in a model BCC multicomponent concentrated solid solution alloy', *Acta Mater*, vol. 125, pp. 311–320, Feb. 2017.
- [44] F. Maresca and W. A. Curtin, 'Mechanistic origin of high strength in refractory BCC high entropy alloys up to 1900K', *Acta Mater*, vol. 182, pp. 235–249, Jan. 2020.
- [45] L. A. Gypen and A. Deruyttere, 'The combination of atomic size and elastic modulus misfit interactions in solid solution hardening', *Scripta Metallurgica*, vol. 15, no. 8, pp. 815–820, Aug. 1981.
- [46] T. Suzuki, 'On the studies of solid solution hardening', *Jpn J Appl Phys*, vol. 20, no. 3, p. 449, Mar. 1981.
- [47] R. Labusch, 'A Statistical Theory of Solid Solution Hardening', *physica status solidi (b)*, vol. 41, no. 2, pp. 659–669, Jan. 1970.
- [48] O. N. Senkov, J. M. Scott, S. v. Senkova, D. B. Miracle, and C. F. Woodward, 'Microstructure and room temperature properties of a high-entropy TaNbHfZrTi alloy', *J Alloys Compd*, vol. 509, no. 20, pp. 6043–6048, May 2011.
- [49] X. Yang and Y. Zhang, 'Prediction of high-entropy stabilized solid-solution in multi-component alloys', *Mater Chem Phys*, vol. 132, no. 2–3, pp. 233–238, Feb. 2012.
- [50] Y. Wu *et al.*, 'Short-range ordering and its effects on mechanical properties of high-entropy alloys', *J Mater Sci Technol*, vol. 62, pp. 214–220, Feb. 2021.

- [51] Y. Rao and W. A. Curtin, 'Analytical models of short-range order in FCC and BCC alloys', *Acta Mater*, vol. 226, Mar. 2022.
- [52] J. C. Fisher, 'On the strength of solid solution alloys', *Acta Metallurgica*, vol. 2, no. 1, pp. 9–10, 1954.
- [53] F. Körmann, A. v. Ruban, and M. H. F. Sluiter, 'Long-ranged interactions in bcc NbMoTaW high-entropy alloys', <http://mc.manuscriptcentral.com/tmrl>, vol. 5, no. 1, pp. 35–40, Jan. 2016.
- [54] Z. Y. Wang, D. Han, and X. W. Li, 'Competitive effect of stacking fault energy and short-range clustering on the plastic deformation behavior of Cu-Ni alloys', *Materials Science and Engineering: A*, vol. 679, pp. 484–492, Jan. 2017.
- [55] D. A. Hardwick, 'Composites Based on Molybdenum Disilicide: Progress and Prospects', *MRS Online Proceedings Library 1994 350:1*, vol. 350, no. 1, pp. 165–176, Dec. 1994.
- [56] P. Tsakiroopoulos, 'Alloys for application at ultra-high temperatures: Nb-silicide in situ composites: Challenges, breakthroughs and opportunities', *Prog Mater Sci*, vol. 123, p. 100714, Jan. 2022.
- [57] L. Jiang *et al.*, 'A Review of Mo-Si Intermetallic Compounds as Ultrahigh-Temperature Materials', *Processes 2022, Vol. 10, Page 1772*, vol. 10, no. 9, p. 1772, Sep. 2022.
- [58] O. N. Senkov, J. K. Jensen, A. L. Pilchak, D. B. Miracle, and H. L. Fraser, 'Compositional variation effects on the microstructure and properties of a refractory high-entropy superalloy AlMo_{0.5}NbTa_{0.5}TiZr', *Mater Des*, vol. 139, pp. 498–511, Feb. 2018.
- [59] J. K. Jensen *et al.*, 'Characterization of the microstructure of the compositionally complex alloy Al₁Mo_{0.5}Nb₁Ta_{0.5}Ti₁Zr₁', *Scr Mater*, vol. 121, pp. 1–4, Aug. 2016.
- [60] V. Soni, O. N. Senkov, B. Gwalani, D. B. Miracle, and R. Banerjee, 'Microstructural Design for Improving Ductility of An Initially Brittle Refractory High Entropy Alloy', *Scientific Reports 2018 8:1*, vol. 8, no. 1, pp. 1–10, Jun. 2018.
- [61] D. B. Miracle, M. H. Tsai, O. N. Senkov, V. Soni, and R. Banerjee, 'Refractory high entropy superalloys (RSAs)', *Scr Mater*, vol. 187, pp. 445–452, Oct. 2020.
- [62] J. P. Couzinié *et al.*, 'High-temperature deformation mechanisms in a BCC+B2 refractory complex concentrated alloy', *Acta Mater*, vol. 233, p. 117995, Jul. 2022.
- [63] O. N. Senkov, C. Woodward, and D. B. Miracle, 'Microstructure and Properties of Aluminum-Containing Refractory High-Entropy Alloys', *JOM*, vol. 66, no. 10, pp. 2030–2042, Oct. 2014.
- [64] V. Soni *et al.*, 'Phase inversion in a two-phase, BCC+B2, refractory high entropy alloy', *Acta Mater*, vol. 185, pp. 89–97, Feb. 2020.
- [65] T. E. Whitfield, E. J. Pickering, K. A. Christofidou, C. N. Jones, H. J. Stone, and N. G. Jones, 'Elucidating the microstructural development of refractory metal high entropy superalloys via the Ti–Ta–Zr constituent system', *J Alloys Compd*, vol. 818, p. 152935, Mar. 2020.
- [66] T. E. Whitfield *et al.*, 'An assessment of the thermal stability of refractory high entropy superalloys', *J Alloys Compd*, vol. 857, p. 157583, Mar. 2021.

- [67] T. E. Whitfield, E. J. Pickering, L. R. Owen, C. N. Jones, H. J. Stone, and N. G. Jones, 'The effect of Al on the formation and stability of a BCC – B2 microstructure in a refractory metal high entropy superalloy system', *Materialia (Oxf)*, vol. 13, p. 100858, Sep. 2020.
- [68] J. P. Abriata and J. C. Bolcich, 'The Nb–Zr (Niobium–Zirconium) system', *Journal of Phase Equilibria* 1982 3:1, vol. 3, no. 1, pp. 34–44, Jun. 1982.
- [69] A. Fernández Guillermet, 'Phase diagram and thermochemical properties of the Zr–Ta system. An assessment based on Gibbs energy modelling', *J Alloys Compd*, vol. 226, no. 1–2, pp. 174–184, Aug. 1995.
- [70] J. L. Li, Z. Li, Q. Wang, C. Dong, and P. K. Liaw, 'Phase-field simulation of coherent BCC/B2 microstructures in high entropy alloys', *Acta Mater*, vol. 197, pp. 10–19, Sep. 2020.
- [71] H. Long *et al.*, 'Effect of lattice misfit on the evolution of the dislocation structure in Ni-based single crystal superalloys during thermal exposure', *Acta Mater*, vol. 120, pp. 95–107, Nov. 2016.
- [72] H. Long *et al.*, 'A comparative study of rafting mechanisms of Ni-based single crystal superalloys', *Mater Des*, vol. 196, p. 109097, Nov. 2020.
- [73] D. Dye, A. Ma, and R. C. Reed, 'NUMERICAL MODELLING OF CREEP DEFORMATION IN A CMSX-4 SINGLE CRYSTAL SUPERALLOY TURBINE BLADE', 2008.
- [74] O. N. Senkov, D. B. Miracle, and S. I. Rao, 'Correlations to improve room temperature ductility of refractory complex concentrated alloys', *Materials Science and Engineering A*, vol. 820, Jul. 2021.
- [75] D. G. Pettifor, 'Theoretical predictions of structure and related properties of intermetallics', <http://dx.doi.org/10.1179/mst.1992.8.4.345>, vol. 8, no. 4, pp. 345–349, 2013.
- [76] D. G. Pettifor, 'New many-body potential for the bond order', *Phys Rev Lett*, vol. 63, no. 22, pp. 2480–2483, 1989.
- [77] S. F. Pugh, 'Relations between the elastic moduli and the plastic properties of polycrystalline pure metals', vol. 45, no. 367, pp. 823–843, Aug. 2009.
- [78] O. N. Senkov and D. B. Miracle, 'Generalization of intrinsic ductile-to-brittle criteria by Pugh and Pettifor for materials with a cubic crystal structure', *Scientific Reports*, vol. 11, p. 4531, 123AD.
- [79] S. Sheikh, S. Shafeie, and Q. Hu, 'Alloy design for intrinsically ductile refractory high-entropy alloys', *J. Appl. Phys*, vol. 120, p. 164902, 2016.
- [80] J. R. Rice and R. Thomson, 'Ductile versus brittle behaviour of crystals', vol. 29, no. 1, pp. 73–97, 2006.
- [81] H. P. Cahn RW, Ed., 'Structure of intermetallic compounds and phases. Physical metallurgy.', 1996.
- [82] T. B. Massalski, 'Comments Concerning Some Features of Phase Diagrams and Phase Transformations', *Mater Trans*, vol. 51, no. 4, pp. 1003151030–1003151030, Apr. 2010.
- [83] U. Mizutani, *Hume-Rothery rules for structurally complex alloy phases*. Available: Hume-Rothery-Rules-for-Structurally-Complex-Alloy-Phases/Mizutani/p/book/9780367383374.

- [84] H. L. Liang, C. W. Tsai, and S. Guo, 'Design of corrosion-resistant high-entropy alloys through valence electron concentration and new PHACOMP', *J Alloys Compd*, vol. 883, p. 160787, Nov. 2021.
- [85] R. Gibala and T. E. Mitchell, 'Solid solution softening and hardening', *Scripta Metallurgica*, vol. 7, no. 11, pp. 1143–1148, Nov. 1973.
- [86] A. Sato and M. Meshii, 'Solid solution softening and solid solution hardening', *Acta Metallurgica*, vol. 21, no. 6, pp. 753–768, Jun. 1973.
- [87] B. v. Petukhov, 'Effect of solid-solution softening of crystalline materials: Review', *Crystallography Reports 2007 52:1*, vol. 52, no. 1, pp. 112–122, Feb. 2007.
- [88] E. Pink and R. J. Arsenault, 'Low-temperature softening in body-centered cubic alloys', *Prog Mater Sci*, vol. 24, no. C, pp. 1–50, Jan. 1980.
- [89] P. Meneses and G. Champier, 'On the Mechanical Behavior of Fe-Mo Alloys', *Journal of the Society of Materials Science, Japan*, vol. 21, no. 231, pp. 1071–1074, Dec. 1972.
- [90] J. R. Stephens and W. R. Witzke, 'Alloy softening in binary iron solid solutions', *Journal of The Less-Common Metals*, vol. 48, no. 2, pp. 285–308, 1976.
- [91] E. Pink, 'LEGIERUNGSENTFESTIGUNG IN KUBISCH-RAUMZENTRIERTEN METALLEN.', *Zeitschrift fuer Metallkunde/Materials Research and Advanced Techniques*, vol. 64, no. 12, pp. 871–881, Dec. 1973.
- [92] R. J. Arsenault, 'Solid solution strengthening and weakening of bcc solid solutions', *Acta Metallurgica*, vol. 17, no. 10, pp. 1291–1297, 1969.
- [93] M. G. Ulitchny, A. A. Sagues, and R. Gibala, 'Alloy softening in niobium-and tantalum-base solid solutions', 1972.
- [94] S. I. Rao, C. Woodward, and B. Akdim, 'Solid solution softening and hardening in binary BCC alloys', *Acta Mater*, p. 118440, Oct. 2022.
- [95] F.G. Coury, 2018, Solid solution strengthening mechanisms in high entropy alloys, PhD thesis, Colorado School of Mines, Golden.
- [96] Y. J. Hu *et al.*, 'Solute-induced solid-solution softening and hardening in bcc tungsten', *Acta Mater*, vol. 141, pp. 304–316, Dec. 2017.
- [97] W. Hume-Rothery and G. Raynor, *The structure of metals and alloys*. 1956.
- [98] W. A. Spitzig and W. C. Leslie, 'Solid-solution softening and thermally activated flow in alloys of Fe with 3at.% Co, Ni or Si', *Acta Metallurgica*, vol. 19, no. 11, pp. 1143–1152, Nov. 1971.
- [99] J. R. Stephens and W. R. Witzke, 'The role of electron concentration in softening and hardening of ternary molybdenum alloys', *Journal of The Less-Common Metals*, vol. 41, no. 2, pp. 265–282, 1975.
- [100] N. I. Medvedeva, Y. N. Gornostyrev, and A. J. Freeman, 'Solid solution softening and hardening in the group-V and group-VI bcc transition metals alloys: First principles calculations and atomistic modeling', *Phys Rev B Condens Matter Mater Phys*, vol. 76, no. 21, p. 212104, Dec. 2007.

- [101] N. I. Medvedeva, Y. N. Gornostyrev, and A. J. Freeman, 'Solid solution softening in bcc Mo alloys: Effect of transition-metal additions on dislocation structure and mobility', *Phys Rev B Condens Matter Mater Phys*, vol. 72, no. 13, p. 134107, Oct. 2005.
- [102] D. R. Trinkle and C. Woodward, 'Materials science: The chemistry of deformation: How solutes soften pure metals', *Science (1979)*, vol. 310, no. 5754, pp. 1665–1667, Dec. 2005.
- [103] M. G. Ulitchny and R. Gibala, 'The effects of interstitial solute additions on the mechanical properties of niobium and tantalum single crystals', *Journal of The Less-Common Metals*, vol. 33, no. 1, pp. 105–116, 1973.
- [104] J. A. Shields, R. Gibala, and T. E. Mitchell, 'Dislocation substructure in Ta-Re-N alloys deformed at 77 K', *Metallurgical Transactions A 1976 7:8*, vol. 7, no. 8, pp. 1111–1121, 197.
- [105] C. Xu and W. Gao, 'Pilling-Bedworth ratio for oxidation of alloys', *Mat. Res. Innovat.*, vol. 3, no. 4, pp. 231–235, 2000.
- [106] 'EllinghamDiagrams'- From Wikipedia.
- [107] C. Leyens and M. Peters, *Titanium and titanium alloys: fundamentals and applications*. 2003.
- [108] S. Sheikh, L. Gan, X. Montero, H. Murakami, and S. Guo, 'Forming protective alumina scale for ductile refractory high-entropy alloys via aluminizing', *Intermetallics*, vol. 123, Aug. 2020.
- [109] Y. Yamamoto *et al.*, 'Creep-resistant, Al₂O₃-forming austenitic stainless steels', *Science (1979)*, vol. 316, no. 5823, pp. 433–436, Apr. 2007.
- [110] P. Tsakiroopoulos, 'Alloys for application at ultra-high temperatures: Nb-silicide in situ composites: Challenges, breakthroughs and opportunities', *Prog Mater Sci*, vol. 123, p. 100714, Jan. 2022.
- [111] B. Gorr, S. Schellert, F. Müller, H. J. Christ, A. Kauffmann, and M. Heilmaier, 'Current Status of Research on the Oxidation Behavior of Refractory High Entropy Alloys', *Adv Eng Mater*, vol. 23, no. 5, p. 2001047, May 202.
- [112] B. Gorr *et al.*, 'Development of oxidation resistant refractory high entropy alloys for high temperature applications: Recent results and development strategy', *Minerals, Metals and Materials Series*, vol. Part F12, pp. 648–659, 2018.
- [113] F. Müller *et al.*, 'On the oxidation mechanism of refractory high entropy alloys', *Corros Sci*, vol. 159, p. 108161, Oct. 2019.
- [114] B. Gorr *et al.*, 'A new strategy to intrinsically protect refractory metal based alloys at ultrahigh temperatures', *Corros Sci*, vol. 166, p. 108475, Apr. 2020.
- [115] P. Kofstad and K. P. Lillerud, 'Chromium transport through Cr₂O₃ scales I. On lattice diffusion of chromium', *Oxidation of Metals*, vol. 17, no. 3–4, pp. 177–194, Apr. 1982.
- [116] N. Birks, G. Meier, and F. Pettit, *Introduction to the high temperature oxidation of metals*. 2006.
- [117] O. A. Waseem, U. Auyes Khan, H. M. Lee, and H. J. Ryu, 'A combinatorial approach for the synthesis and analysis of Al_xCryMozNbTiZr high-entropy alloys: Oxidation behavior', *J Mater Res*, vol. 33, no. 19, pp. 3226–3234, Oct. 2018.

- [118] T. M. Butler and M. L. Weaver, 'Oxidation behavior of arc melted AlCoCrFeNi multi-component high-entropy alloys', *J Alloys Compd*, vol. 674, pp. 229–244, Jul. 2016.
- [119] X. Yang *et al.*, 'Effect of Al content on the thermal oxidation behaviour of AlHfMoNbTi high-entropy alloys analysed by in situ environmental TEM', *Corros Sci*, vol. 191, p. 109711, Oct. 2021.
- [120] 'ISO - ISO 6507-1:2005 - Metallic materials — Vickers hardness test — Part 1: Test method'. <https://www.iso.org/standard/37746.html>.
- [121] 'Crystallography and Crystal Defects - Anthony Kelly, Kevin M. Knowles.
- [122] J. Goldstein, *Practical scanning electron microscopy: electron and ion microprobe analysis*. 2012.
- [123] G. Taylor, 'Thermally-activated deformation of BCC metals and alloys', *Prog Mater Sci*, vol. 36, pp. 29–61, Jan. 1992.
- [124] F. G. Coury, 'Solid solution Strengthening in HEAs', *Thesis*, pp. 1–140, 2018.